Impact of upper mantle convection on lithosphere hyper-extension and subsequent convergence-induced subduction

Lorenzo G. Candioti[1], Stefan M. Schmalholz[1], and Thibault Duretz[1,2]

[1]Institut des sciences de la Terre, Bâtiment Géopolis, Quartier UNIL-Mouline, Université de Lausanne, 1015 Lausanne (VD), Switzerland
[2]Univ.-Rennes, Rennes, France

Correspondence: Lorenzo G. Candioti (Lorenzo.Candioti@unil.ch)

Abstract.

   We present two-dimensional thermo-mechanical numerical models of coupled lithosphere-mantle deformation, considering the upper mantle down to a depth of 660 km. We consider visco-elasto-plastic deformation and for the lithospheric and upper mantle a combination of diffusion, dislocation and Peierls creep. Mantle densities are calculated from petrological phase
5 diagrams (Perple_X) for a Hawaiian pyrolite. The model generates a 120 Myrs long geodynamic cycle of subsequent extension (30 Myrs), cooling (70 Myrs) and convergence (20 Myrs) in a single and continuous simulation with explicitly modelling convection in the upper mantle. During lithosphere extension, the models generate an approximately 400 km wide basin of exhumed mantle bounded by hyper-extended passive margins. The models show that considering only the thermal effects of upper mantle convection by using an effective thermal conductivity generates results of lithosphere hyper-extension that are
10 similar to the ones of models that explicitly model the convective flow. Applying a lower viscosity limit of 5×10^{20} Pa s suppresses convection and generates results different to the ones for simulations with a low viscosity asthenosphere having minimal viscosity of approximately 10^{19} Pa s. During cooling without far-field deformation, no subduction of the exhumed mantle is spontaneously initiated. Density differences between lithosphere and mantle are too small to generate a buoyancy force exceeding the mechanical strength of the lithosphere. The extension and cooling stages generate self-consistently a
15 structural and thermal inheritance for the subsequent convergence stage. Convergence initiates subduction of the exhumed mantle at the transition to the hyper-extended margins. The main mechanism of subduction initiation is thermal softening for a plate driving force (per unit length) of approximately 15 TN m^{-1}. If convection in the mantle is suppressed by high effective thermal conductivities or high, lower viscosity limits, then subduction initiates at both margins leading to divergent double-slab subduction. Convection in the mantle assists to generate a single-slab subduction at only one margin, likely due to mantle flow
20 which exerts an additional suction force on the lithosphere. The first-order geodynamic processes simulated in the geodynamic cycle of subsequent extension, cooling and convergence are applicable to orogenies that resulted from the opening and closure of embryonic oceans bounded by magma-poor hyper-extended passive margins, which might have been the case for the Alpine orogeny.

1 Introduction

Heat transfer through the lithosphere is dominated by thermal diffusion while heat transfer through the underlying mantle is dominated by convection (e.g. Turcotte and Schubert, 2014). Over long-term ($> \approx 80$ Myrs) geodynamic time scales, convection below the lithosphere maintains a more or less constant thermal thickness and heat flow across the lithosphere, and hence regulates and stabilises the thermal structure of the lithosphere (Richter, 1973; Parsons and McKenzie, 1978). Consequently, convection in the mantle exerts a strong control on the thermal history, and consequently on the strength, of the lithosphere. Historically, ignoring convection was the main reason why early estimates of the age of the Earth, based on thermal diffusion only, provided estimates that were two orders of magnitude too young; it was not because of ignoring radioactive heat production (England et al., 2007).

Many coupled lithosphere-mantle deformation processes are still incompletely understood, such as the formation of hyperextended passive margins (e.g. Peron-Pinvidic et al., 2019) or the initiation of subduction (e.g. Stern and Gerya, 2018). In addition to field and laboratory studies, theoretical studies, often employing numerical simulations, have proven useful to understand and quantify these processes. Many numerical studies modelling the deformation of the lithosphere and the underlying mantle, or thinner asthenosphere, do not directly model convective flows below the lithosphere (e.g. Jaquet and Schmalholz, 2018; Beaussier et al., 2019; Erdös et al., 2019; Li et al., 2019). Ignoring convection below the lithosphere in numerical simulations is likely not problematic if the duration of the simulated deformation is not exceeding a few tens of millions of years, because in such short time interval the diffusive cooling of the lithosphere is likely negligible. However, many studies show that geodynamic processes are embedded in longer term cycles, such as the Wilson cycle (Wilson, 1966; Wilson et al., 2019), and that tectonic inheritance of earlier extension and cooling events had presumably a major impact on subsequent convergence and subduction evolution (Chenin et al., 2019). To investigate and quantify the coupled lithosphere-mantle deformation processes during such long-term geodynamic cycles with numerical models, requires, in principle, that these models consider convection in the mantle. However, modelling convection in the mantle directly in numerical models focusing on lithosphere deformation is computationally challenging since the convection in the mantle must be spatially and temporally resolved. A common approach to indirectly include the thermal effects of mantle convection into numerical simulations, without actually modelling the velocity field of the convection, is to use an effective thermal conductivity parameterization (Zahnle et al., 1988) (see also appendix B). This approach has been used, for example, in mantle convection studies for planetary bodies when the convection of the mantle is too vigorous to be modelled explicitly (e.g. Zahnle et al., 1988; Tackley et al., 2001; Golabek et al., 2011), in models of back-arc lithospheric thinning through mantle flow that is induced by subduction of an oceanic plate (e.g. Currie et al., 2008), or in models of lithosphere extension and subsequent compression (e.g. Jammes and Huismans, 2012). A main parameter controlling the vigour of upper mantle convection is the effective viscosity. The larger the viscosity the smaller the convection velocities and, with respect to numerical simulations, the larger is also the admissible time step and the smaller the number of total time steps. However, compared to the density and thermal structures, the viscosity structure of the upper

mantle is subject to large uncertainty, because it is not directly observable and can only be inferred by inverting observable geophysical data such as data for glacial isostatic adjustment (e.g. Mitrovica and Forte, 2004)) or seismic anisotropy data (e.g. Behn et al., 2004). Especially at depths of ca. 100-300 km, within the asthenosphere, the inferred value for viscosity varies greatly (see fig. 2 in Forte et al. (2010)) and can be up to two orders of magnitude lower than estimates for the average upper mantle viscosity of $\approx 10^{21}$ Pa s (Hirth and Kohlstedt, 2003; Becker, 2017). Furthermore, mantle convection does not only impact the thermal structure of the lithosphere but can also exert suction forces due to mantle flow on the lithosphere (e.g. Conrad and Lithgow-Bertelloni, 2002). For example, numerical simulations show that suction forces due to mantle flow can assist in the initiation of subduction (Baes et al., 2018). Currently, the impact of convection in the upper mantle on the long term deformation cycles of the lithosphere is not well understood.

Here, we simulate numerically a long-term (>100 Myrs) geodynamic cycle of subsequent lithosphere extension, cooling without far-field deformation and convergence causing subduction initiation, and consider convection in the upper mantle. We refer here to the region between the lithosphere and the density discontinuity at 660 km depth as upper mantle. We quantify the impact of different viscosity structures and of applying an effective thermal conductivity on upper mantle convection and coupled lithosphere deformation. For simplicity, we consider lithosphere extension that generates magma-poor hyper-extended margins and crustal separation leading to mantle exhumation so that we do not need to model melting, lithosphere break-up, mid-ocean ridge formation and generation of new oceanic crust and lithosphere. Such Wilson-type cycles, involving only embryonic oceans, presumably formed orogens such as the Pyrenees, the Western and Central Alps, and most of the Variscides of Western Europe (e.g. Chenin et al., 2019). We present two-dimensional (2D) thermo-mechanical numerical simulations in which convection in the upper mantle is (1) directly modelled and numerically resolved, (2) slowed down by a viscosity cut-off and (3) indirectly considered by applying a high effective thermal conductivity. In addition to testing the impact of convection, another aim of modelling an entire extension-cooling-convergence-subduction cycle is to test whether the applied numerical algorithm can generate the first order features of such a cycle within a single and continuous numerical simulation. These first order features are: (1) formation of hyper-extended passive margins, (2) separation of the continental crust and exhumation of mantle material, (3) upper mantle convection stabilizing the thermal thickness of the lithosphere and heat flow at its base and (4) subduction initiation during convergence. A further aim of modelling such cycle is to test whether convergence-induced subduction at passive margins can occur in a self-consistent way without prescribing ad-hoc a prominent weak zone across the lithosphere. We also investigate whether velocities and forces in the upper mantle associated to convection have an impact on convergence-induced subduction.

2 Model

2.1 Mathematical model

We use 2D numerical thermo-mechanical simulations to investigate coupled lithosphere and mantle deformation during a geodynamic cycle of extension, cooling and subsequent convergence. The applied code solves the partial differential equations for deformation of incompressible visco-elasto-plastic slowly (no inertia) flowing fluids under gravity coupled with energy

90 conservation. The equations are discretized on a 2D finite difference staggered grid in the Cartesian coordinate system. Material properties are advected using a marker-in-cell method (Gerya and Yuen, 2003). A 4th order Runge-Kutta scheme is employed for marker advection and a true free surface is applied (Duretz et al., 2016). A detailed description of the algorithm is given in the appendix A. A convection benchmark of the applied algorithm is presented in appendix C.

2.2 Model configuration

95 The model domain is 1600 km wide and 680 km high and the applied model resolution is 801×681 grid points (fig. 1). The top surface is stress free (free surface, see Duretz et al. (2016a)) and thus evolves dynamically throughout the model evolution. Mechanical boundary conditions on the remaining boundaries are set to free slip at the bottom, free slip with constant material inflow/outflow velocities at the left and right boundary. The boundary velocity is calculated such that the total volume of material flowing through the lateral boundary is conserved. The transition between inflow and outflow occurs

100 at half of the model height. Initial temperature at the surface is set to 15 °C and temperatures at the crust-mantle (Moho) and at the lithosphere-asthenosphere boundaries (LAB) are 600 °C and 1350 °C, respectively. Assuming an adiabatic gradient of 0.49 °C/km, the temperature at the model bottom is 1612 °C. Thermal boundary conditions are set to isothermal at the bottom and at the top of the domain and the left and right boundary are assumed to be insulating, i.e. no heat flows through lateral boundaries. Model units include a 33 km thick, mechanically layered crust which overlies an 87 km thick mantle lithosphere on top of

105 the upper mantle. The crust includes three mechanically strong and four mechanically weak layers of 5 km thickness each. Mechanical layering of the crust was chosen because it is a simple way of considering heterogeneities in the crust that lead to more realistic hyper-extended passive margin geometries during rifting (Duretz et al., 2016b). To localize the deformation in the horizontal center of the model, we perturbed the initially flat layer interfaces with a random vertical displacement, within the x-position -75 and 75 km. The magnitude of the vertical displacement is in average approximately 1 km. The viscosity

110 of all model units is a combination of several flow laws including, dislocation creep for the crustal units and dislocation, diffusion and Peierls creep for lithospheric mantle and the upper mantle. The initial viscosity profile through the upper mantle is calibrated to match viscosity data obtained by Ricard et al. (1989). The applied flow law parameters lie within the error range of the corresponding laboratory flow law estimates. The difference between mantle lithosphere and upper mantle is temperature only, i.e. all material parameters are the same. Density of the crustal phases is computed with a simple equation of state (eq.

115 A3), whereas density of the mantle phase is pre-computed using Perple_X (Connolly, 2005) for the bulk rock composition of a pyrolite (Workman and Hart (2005), fig. A1). A detailed description of the phase transitions and how the initial thermal field is calibrated is given in appendix B. Surface processes (e.g., erosion and sedimentation) are taken into account by a kinematic approach: if the topography falls below a level of 5 km depth or rises above 2 km height, it undergoes either sedimentation or erosion with a constant velocity of 0.5 mm yr^{-1} within one numerical time step. In case of sedimentation, the generated cavity

120 between the old and corrected topographic level is filled with sediments, alternating between calcites and pelites every 2 Myrs.

Three subsequent stages of a geodynamic cycle are modelled in one continuous simulation: (1) Opening of a ca. 360 km wide marine basin floored by exhumed mantle and bounded by hyper-extended passive margins during a 30 Myrs extension period applying an absolute extension velocity of 2 cm yr^{-1}, (2) a 70 Myrs thermal relaxation period applying no far-field

Table 1. Parameters used in models M1-6.

Parameter	Unit	M1	M2	M3	M4	M5	M6
k_{th}	$\text{W m}^{-1}\,\text{K}^{-1}$	2.75	36	2.75	36	2.75	2.75
η_{cutoff}	Pa s	1×10^{18}	1×10^{18}	1×10^{20}	1×10^{20}	5×10^{20}	1×10^{18}
Ra_{avg}	-	2.2×10^{6}	4.4×10^{5}	8.8×10^{5}	1.2×10^{5}	2.7×10^{5}	5.0×10^{7}
Rheology mantle	-	Dry Olivine	Dry Olivine	Dry Olivine	Dry Olivine	Dry Olivine	Wet Olivine

k_{th} is thermal conductivity and η_{cutoff} is the lower viscosity limiter. Ra_{avg} is the average Rayleigh number computed for the models M1-5 at the end of the cooling period and for M6 at the end of the rifting period according to eq. B1. The upper most ca. 90 km of the model domain are not included in the arithmetic mean calculation for averaging.

deformation and (3) a 20 Myrs convergence period in which the self-consistently evolved passive margin system is shortened applying an absolute convergence velocity of $3\,\text{cm yr}^{-1}$. Figure 1 shows the initial configuration of the models.

We perform three types of simulations to investigate the impact of upper mantle convection on lithosphere deformation: (1) explicitly modelling and numerically resolving the convection for a viscosity structure with a weak asthenosphere, (2) parameterizing convection, without explicitly modelling convective flow, by scaling the thermal conductivity to the Nusselt number of upper mantle convection (see app. B) and (3) quantifying the impact of different viscosity structures of the upper mantle. We perform a set of 6 simulations, which will be named M1-6 hereafter. M1 is defined as the reference model in which the process of convection is explicitly modelled and numerically resolved for a weak asthenosphere. M2 is equivalent to M1, except that the impact of convection on the thermal field is investigated using an effective conductivity. M3 and M4 are equivalent to M1 and M2, but the viscosity is limited to a minimum value of $10^{20}\,\text{Pa s}$. In M5, the viscosity is limited to a minimum value of $5\times10^{20}\,\text{Pa s}$ using a realistic value for thermal conductivity in the upper mantle. Mantle material in M1-5 is described using flow law parameters for a dry olivine rheology. In M6, the material parameters of the dislocation and diffusion creep mechanism of a dry olivine rheology are replaced by the parameters for a wet olivine rheology (table 2). Within the error range of values for activation volume and energy of the wet olivine rheology, the viscosity is calibrated to the data obtained by Ricard et al. (1989). However, using the highest possible values for the wet olivine flow law parameters, the maximum viscosity in the upper mantle is one order of magnitude lower compared to models M1-5. In M1,2 and M6, we apply a lower viscosity cut-off at $10^{18}\,\text{Pa s}$. A summary of all simulations is given in table 1 and all material parameters are summarised in table 2.

3 Results

We describe here the results of M1-5 for the subsequent extension, thermal relaxation and convergence stages. We describe results of M6 for the extension stage only because its later evolution is not applicable to Earth due to unrealistic Moho temperatures and mantle viscosities.

Table 2. Physical parameters used in the numerical simulations M1-6.

Parameter	Unit	Strong Crust[1]	Weak Crust[2]	Sediments[3]	Sediments[4]	Dry Mantle[5,6]	Wet Mantle[5,6]
ρ_0	kg m^{-3}	2800	2800	2800	2800	-	-
G	Pa	2×10^{10}	2×10^{10}	2×10^{10}	2×10^{10}	2×10^{10}	2×10^{10}
c_P	J kg^{-1} K^{-1}	1050	1050	1050	1050	1050	1050
k	W m^{-1} K^{-1}	2.25	2.25	2.37	2.55	2.75	2.75
H_R	W m^{-3}	0.9×10^{-6}	0.9×10^{-6}	0.56×10^{-6}	2.9×10^{-6}	2.1139×10^{-8}	2.1139×10^{-8}
C	Pa	10^7	10^6	10^7	10^6	10^7	10^7
φ	°	30	5	30	5	30	30
α	K^{-1}	3×10^{-5}	3×10^{-5}	3×10^{-5}	3×10^{-5}	3×10^{-5}	3×10^{-5}
β	Pa^{-1}	1×10^{-11}	1×10^{-11}	1×10^{-11}	1×10^{-11}	1×10^{-11}	1×10^{-11}
Dislocation							
A	Pa^{-n-r} s^{-1}	5.0477×10^{-28}	5.0717×10^{-18}	1.5849×10^{-25}	10^{-138}	1.1×10^{-16}	5.6786×10^{-27}
n	-	4.7	2.3	4.7	18	3.5	3.5
Q	J mol^{-1}	485×10^3	154×10^3	297×10^3	51×10^3	530×10^3	460×10^3
V	m^3 mol^{-1}	0	0	0	0	14×10^{-6}	11×10^{-6}
r	-	0	0	0	0	0	1.2
$f_{\mathrm{H_2O}}$	Pa	0	0	0	0	0	10^9
Diffusion							
A^*	Pa^{-n-r} m^m s^{-1}	-	-	-	-	1.5×10^{-15}	2.5×10^{-23}
n	-	-	-	-	-	1	1
Q	J mol^{-1}	-	-	-	-	370×10^3	375×10^3
V	m^3 mol^{-1}	-	-	-	-	7.5×10^{-6}	20×10^{-6}
m	-	-	-	-	-	3	3
r	-	-	-	-	-	0	1
$f_{\mathrm{H_2O}}$	Pa	-	-	-	-	0	10^9
d	m	-	-	-	-	10^{-3}	10^{-3}
Peierls							
A_P	s^{-1}	-	-	-	-	5.7×10^{11}	5.7×10^{11}
Q	J mol^{-1}	-	-	-	-	540×10^3	540×10^3
σ_P	Pa	-	-	-	-	8.5×10^9	8.5×10^9
γ	-	-	-	-	-	0.1	0.1

Flow law parameters are taken from: [1]Mackwell et al. (1998), [2]Ranalli (1995), [3]Schmid et al. (1977), [4]Kronenberg et al. (1990), [5]Hirth and Kohlstedt (2003) and [6]Goetze and Evans (1979), regularised by Kameyama et al. (1999). [*]Converted to SI units from original units:

$A = 2.5 \times 10^7 \, ([\mathrm{MPa}])^{-n-r} \, ([\mathrm{\mu m}])^m \, ([\mathrm{s}])^{-1} = 2.5 \times 10^7 \times (10^{-6n-6r} \, [\mathrm{Pa}]^{-6n-6r}) \times (10^{-6m} \, [\mathrm{m}]^m) \times ([s]^{-1}) = 2.5 \times 10^{-23} \, [\mathrm{Pa}^{-2}\mathrm{m}^3\mathrm{s}^{-1}]$.

3.1 Extension

3.1.1 Dry Olivine rheology: Models M1-5

After 13 Myrs of extension M1-4 produce two conjugate asymmetric hyper-extended margins (c.f. 2(a)-(e)). In M1 and M2, the left continental margin has a length of ca. 200 km and the right margin has a length of ca. 150 km (fig. 2(a) & (b)). Both margins of M3 and M4 are approximately 150 km long (fig. 2(c) & (d)). The two margins of M5 are connected by a long zone of hyper-extended crust (i.e., its thickness is less than 10 km) and crustal break-up does not occur (fig. 2(e)) up to this stage.

In none of the simulations the 1350 °C isotherm comes closer than 30 km to the surface. The viscosity of the upper mantle decreases to minimal values around 10^{19} Pa s and increases again up to values in the order of 10^{21} Pa s at the bottom of the model domain in M1 and M2. In M3, M4 and M5 the minimal value for effective viscosity in the upper mantle is at the applied cut-off value of 1×10^{20} Pa s and 5×10^{20} Pa s and increases up to values in the order of 10^{21} Pa s at a depth of 660 km (see fig. 5(c) & 2(c)-(e)). Horizontally averaged vertical temperature profiles are similar in all the models (fig. 5(a) & (g)). The level of the 1350 °C isotherm remains at its initial depth in M2 and M4, whereas it subsides by ca. 20 km in M1, M3 and M5. Horizontally averaged, density profiles (fig. 5(b)) show density differences <10 kg m^{-3} between ca. 35 km and ca. 120 km depth.

The vertically integrated second invariant of the deviatoric stress tensor, $\bar{\tau}_{\mathrm{II}}$, is a measure for the strength of the lithosphere and twice its value is representative for the horizontal driving force (per unit length) during lithosphere extension and compression (appendix D). During the pure shear thinning phase in the first ca. 2 Myrs of extension, values for $2 \times \bar{\tau}_{\mathrm{II}}$ (fig. 8(d)) reach 14 TN m^{-1}. At ca. 2-3 Myrs, values for $2 \times \bar{\tau}_{\mathrm{II}}$ decrease below ca. 5 TN m^{-1}. At the end of the extension period the values for $2 \times \bar{\tau}_{\mathrm{II}}$ stabilise between ca. 2-3 TN m^{-1} for all models.

3.1.2 Wet Olivine rheology: Model M6

M6 does not reach the stage of crustal break-up (fig. 3(a)-(d)) within 30 Myrs. Both margins are connected by an approximately 100 km wide zone of hyper-extended crust (fig. 3(c)). Values for effective viscosity in the upper mantle decrease to minimal values around 10^{19} Pa s at a depth of 660 km in the early stage of the model evolution (fig. 3(a)). The mantle lithosphere delaminates, indicated by a rising level of the 10^{21} Pa s contour in fig. 3(a)-(d). Values for viscosity in the entire upper mantle and transition zone fall to the applied lower viscosity limit of 10^{18} Pa s. After 26 Myrs in model history, the majority of the mantle lithosphere has been delaminated (see level of 10^{21} Pa s contour in fig. 3(d)). Values for temperature at the Moho reach ca. 1000 °C.

3.2 Thermal relaxation

At the end of the thermal relaxation period (ca. 99 Myrs), M1 develops convection cells in the upper mantle. The size of the cells varies between ca. 50 km and ca. 300 km in diameter below the left and right margin respectively (fig.4(a)). Vertical velocities are ca. 1-1.5 cm yr^{-1}. Below the right margin a downward directed material flow with ca. 2-3 cm yr^{-1} develops (see

dark blue cell at ca. +300 km in horizontal x-direction in fig.4(a)). At a depth of ca. 120 km a laterally heterogeneous horizontal mantle flow field develops (fig. 4(f)) showing a region of convergent flow directions below the right margin. Absolute values for velocities of mantle flow are ca. 2 cm yr^{-1}. Material transport in M2 and M4 occurs with velocities below ca. 0.5 cm yr^{-1}

180   (fig. 4(b),(d),(g),(i)). Essentially no convection cells develop in these models (see undeflected 1350 °C and 1450 °C isotherms in fig. 4(b) & (d)). The size of the convection cells in M3 is in the order of ca. 100-300 km in diameter. The cell size and the magnitude of material flow velocity are distributed horizontally symmetric below both margins (fig.4(c) & (h)). A zone of strong downward directed movement with > 2 cm yr^{-1} develops (dark blue cells at ca. -300 km and ca. +300 km in horizontal x-direction in fig.4(c)) below both margins. M5 develops two zones where the lithosphere is delaminating. Downward directed

185   movement of material occurs with ca. 2 cm yr^{-1} (darker blue regions at ca. -500 km and ca. 500 km in horizontal x-direction in fig.4(d)).

All models maintain a stable lithospheric thickness of 90-100 km over 100 Myrs (magenta viscosity contour in fig. 4) and no thermal erosion of the lithosphere occurs. Horizontally averaged temperature profiles remain similar for M1-5 (fig. 5(d)). Figure 10 shows the conductive heat flow of the entire domain in absolute values. M1-5 reproduce a heat flux of 20-30 mW

190   m^{-2} through the base of the lithosphere (indicated by the 10^{21} Pa s isopleth at a depth between 100-110 km). The conductive heat flow below the lithosphere is close to 0 mW m^{-2} in M1, M3 and M5. In M2 and M4 values for conductive heat flow remain at ca. 20 mW m^{-2} in the upper mantle. Density differences in the upper part of the mantle lithosphere reach ca. 20 kg m^{-3} between ca. 35-120 km in depth (fig. 5(h) & (j)). Values for effective viscosity range in the order of 10^{19} Pa s in the upper mantle diretcly below the lithosphere and 10^{21} Pa s at the bottom of the upper mantle (fig. 5(f)).

195   Values of $2 \times \bar{\tau}_{II}$ remain constant at values between 2.5-3.0 TN m^{-1} for all models during the entire thermal relaxation period (fig. 8(d)). Because no far-field deformation is applied during the thermal relaxation, the stresses result only from convective flow and from lateral variations of gravitational potential energy (GPE) between elevated regions with continental crust and lower ones with exhumed mantle.

3.3 Convergence and subduction

200   Figure 8(a) shows the topography at ca. 102 Myrs in model history, that is 2 Myrs after the start of convergence. Topography does not exceed 1.5 km and the average depth of the basin is ca. 4 km. In M1 and M2, a single, major shear zone develops in the lithosphere at the right continental margin (fig. 6(a) & (b)). The strain rate distribution is asymmetric (fig.6(a) & (b)). In M3-5 two major symmetric shear zones develop in the lithosphere, one shear zone at each of the continental margins (fig.6(c)-(e)). At this early stage of subduction initiation, the strain rate in the shear zone is in the order 10^{-13} s^{-1}. In the region of the shear

205   zones, the temperature is increased, which is indicated by the deflection of the isotherms (red contour lines in fig.6(a)-(e)). Convection is still active in the upper mantle in M1 (strain rate distribution below viscosity contour in fig. 6(a)). Horizontal profiles of GPE show increasing symmetry from M1 to M5 (fig. 8(c)), but the profiles are in general similar. Figure 8(b) shows a horizontal profile of the vertical velocity at 175 km depth indicating a significant lateral asymmetry in M1. Magnitudes of vertical velocity reach ca. -3 cm yr^{-1} at x-position of ca. 300 km. The vertical velocities are three times lower below the other

210   margin. The distribution of vertical velocity in M2-5 is laterally symmetric. Minimal values of approximately -2 cm yr^{-1} are

reached in M2, M3 and M4 (red and black dashed lines in fig. 8), whereas in M5 minimal values of vertical velocity are ca. -1 cm yr^{-1}. Values of $2\times\bar{\tau}_{II}$ reach maximum values of ca. 22 TN m^{-1} in M5 and range between 12-20 TN m^{-1} in M1-4 (fig. 8(d)).

215   In M1, one stable subduction zone develops below one of the continental margins and a trench forms in which sediments are deposited (fig.7(a)). Folding of the crustal layers in the overriding plate indicates significant deformation of the crust. The crustal layers of the subducting plate remain relatively undeformed. The viscosity in the upper mantle remains stable at values of 10^{19} Pa s during the entire model history. Also, the thermal thickness of the lithosphere remains stable and relatively constant over time. In M2-5, subduction is initiated below both margins and sediments are deposited in two trenches (fig.7(b)-(e)). Alternating activity of the subduction zones is observed. Folding of the crustal layers indicates deformation in both margins.
220   Values for viscosity in the upper mantle remain stable at values of 10^{19} Pa s in M2, whereas the viscosity values are at the applied lower cut-off value in M3-5 throughout the entire simulation history. Subduction initiation and strain localization at ca. 102 Myrs is associated with a rapid decrease of $2\times\bar{\tau}_{II}$ whereby values of $2\times\bar{\tau}_{II}$ decrease by ca. 2-5 TN m^{-1} in all models. At ca. 105 Myrs, values of $2\times\bar{\tau}_{II}$ increase again until the end of the simulation as shown in fig. 8(b). At this stage the vertical velocity field of M1 shows only one active convection cell (fig. 9(a)). Convection is not active in M4 (cf. fig. 9(b)&(e)). The
225   10^{21} Pa s viscosity isopleth remains at a constant depth away from the subduction zone.

4   Discussion

4.1   Extension

Higher values for the lower viscosity cut-off (M3 compared to M1) decrease the mechanical heterogeneity in the crust. In consequence, the multi-layered crust necks effectively as a single layer. The resulting passive margins are shorter and more
230   symmetric (Chenin et al., 2017, see also M3). The highest cut-off value of 5×10^{20} (M5) leads to a two-stage necking as investigated by Huismans and Beaumont (2011): first, the lithosphere is necking while the crust deforms by more or less homogeneous thinning, leading to the development of a large continuous zone of hyper-extended crust, below which the mantle lithosphere has been removed. Second, the hyper-extended crust is breaking up after the continental mantle lithosphere. Mantle convection does not establish as early as rifting and crustal separation. Therefore, the evolution of M1-4 is similar
235   and the effective conductivity approach (M2, M4) leads to similar margin geometries as predicted by the realistic conductivity model (M1, M3).

In our models, we drive extension with horizontal boundary velocities that are constant during extension. Another end-member boundary condition is to assume a lateral constant extensional force (e.g. Brune et al., 2016). These different boundary conditions likely have a significant impact on the extensional evolution, but quantifying the impact of these boundary conditions
240   is beyond the scope of our study.

4.2 Thermal relaxation

Vigour of the convecting system is described by its Rayleigh number. The average Rayleigh number (see appendix eq.B1) in M1 is ca. 2×10^6 (see tab. 1) which is in the range of realistic values for upper mantle convection (Torrance and Turcotte, 1971). Heat flow through the lithosphere at a depth slightly above the convecting cells (ca. 100-110 km) is between 20-30 mW m^{-2} (fig. 10(a)) which is in the range of realistic values for heating at the base of the lithosphere confirmed by other numerical studies (Turcotte and Schubert, 2014; Petersen et al., 2010). Below the lithosphere the conductive heat flux is essentially zero, because heat transport is mainly due to advection of material in the convecting cells. M3 and M5 produce similar values for the conductive heat flux as M1. The main difference between M1, M3 and M5 is the speed at which material is transported: values for the Rayleigh number in M3 and M5 are ca. one order of magnitude lower compared to M1 (see tab. 1), because the higher viscosity limit raises values for viscosity in the upper mantle. The limited velocities in the upper mantle reduce the total number of time steps needed for the computation by ca. a factor 1.3 for M3 and by ca. a factor 3.5 for M5 compared to the total number of time steps computed for M1. In M2 and M4, the Rayleigh number is also ca. one order of magnitude lower compared to M1 (see table 1), due to the high effective thermal conductivity (included in κ in eq. B1), which reduces the total number of time steps by a factor of 1.8 and 3.0 for M2 and M4, respectively, compared to M1. Although the effective conductivity approach maintains a reasonable heat flux at the base of the lithosphere (figs. 10(b) & (d)) all processes in the upper mantle are conduction dominated. This results in values for the Rayleigh and Nusselt number of the system which are not representative for the Earth's mantle convection.

Cloos (1993) proposed that the density increase of cooling oceanic lithosphere compared to the underlying asthenosphere is in the order of 80 kg m^{-3}. According to Cloos (1993), this difference is sufficient to initiate subduction spontaneously by negative buoyancy of the oceanic lithosphere (see Stern (2004); Stern and Gerya (2018, & references therein) for detailed explanation). However, McKenzie (1977) and Mueller and Phillips (1991) showed using analytical solutions that the forces acting on the lithosphere due to buoyancy contrasts are not high enough to overcome the strength of the cold oceanic lithosphere. Observations of old plate ages (>100 Myrs) around passive margins in the South Atlantic indicate long-term stability of old oceanic lithosphere. In the models presented here, the applied thermodynamic density of the Hawaiian pyrolite leads to density differences between the exhumed mantle in the basin and the underlying asthenosphere of ca. 10-20 kg m^{-3} across a vertical distance of 85 km after 99 Myrs in model history. Compared to the buoyancy contrast proposed by Cloos (1993) the density differences presented here are by a factor 4 smaller, which is, however, consistent with more recent estimates presented by Afonso et al. (2007). Boonma et al. (2019) report a density difference of +19 kg m^{-3} for an 80 km thick continental lithosphere and +17 kg m^{-3} for an oceanic lithosphere of 120 Myrs of age, which is in agreement with the values we report in our study. In the 2D models presented here, these buoyancy contrasts are insufficient to overcome the internal strength of the cooled oceanic lithosphere and initiate subduction spontaneously. Our results are, hence, in agreement with the stability of old oceanic lithosphere in, for example, the South Atlantic, where even an additional ridge push of approximately 3.9 TN m^{-1} (Turcotte and Schubert, 2014) was not sufficient to initiate subduction.

4.3 Subduction

275 Figure 8(a) shows the topographic elevation at the stage of subduction initiation. In all models, the difference between the lowest point in the trenches and the highest point of the margins is ca. 5 km which is predicted by the principle of isostasy for a ca. 30 km thick crust with an average density of 2800 $\mathrm{kg\,m^{-3}}$ (Turcotte and Schubert, 2014). Therefore, the models are in a state of isostatic equilibrium at the onset of subduction initiation.

Currently, the processes leading to subduction initiation remain elusive (Stern, 2004; Stern and Gerya, 2018; Crameri et al.,

280 2019). Stern (2004) proposed two fundamental mechanisms for subduction initiation: (1) spontaneous and (2) induced subduction initiation. Spontaneous subduction initiation occurs, for example, due to densification of the oceanic lithosphere during secular cooling. Induced subduction initiation occurs, for example, due to far-field plate motion. In fact, many numerical studies that investigate subduction processes do not model the process of subduction initiation. In these studies, either a major weak zone across the lithosphere is prescribed ad-hoc in the initial model configuration to enable subduction (Ruh et al., 2015; Zhou

285 et al., 2020) or the initial model configuration includes already a prescribed slab so that subduction has already initiated at the onset of the simulation (Kaus et al., 2009; Garel et al., 2014; Dal Zilio et al., 2018). In our models, subduction is initiated self-consistently, without prescribing any major weak zone or an already existing slab. The model geometry and temperature field at the onset of convergence were also simulated in a self-consistent way by the previous modelling of extension and thermal relaxation. During convergence, shear heating together with the temperature and strain rate dependent viscosity formulation

290 (dislocation creep flow law, eq. A6) causes the spontaneous generation of a lithosphere-scale shear zone that evolves into a subduction zone (Thielmann and Kaus, 2012; Kiss et al., 2020). However, shear heating is a transient process which means the increase in temperature is immediately counterbalanced by thermal diffusion. Efficiency of shear heating is restricted to the first ca. 2-3 Myrs after shear zone formation in the presented models. After this time span, heat generated by mechanical work is diffused away and single-slab subduction may not be stable anymore (see M2-5). This means that long-term occur-

295 rence of a single-slab subduction in M1 is likely caused by a different mechanism than shear heating. Figure 8(c) shows the difference in GPE. The horizontal profiles do not reveal significant differences between the models. The GPE is sensitive to topography and density distribution throughout the model domain. The convection induced heterogeneity in the density field of the upper mantle are confined to a thin layer and the magnitude of these differences is only ca. 10-20 $\mathrm{kg\,m^{-3}}$. When integrated over the entire depth, such variations do not significantly impact the GPE profiles. Instead, the signal reflects the topography,

300 which is similar in all the models due to the similar margin geometry (see fig. 8(a) and fig. 2(a)-(e)). However, the horizontal profile at a depth of 175 km of the vertical velocity (fig. 8(b)) reveals a possible explanation for why single-slab subduction is stable in M1. The increased lateral heterogeneity in the upper mantle is inherited from the convection active during the thermal relaxation period. The vertical velocity field at the end of the thermal relaxation period of M1 (fig. 4(a)) reveals a zone of convection with velocities in the order of the convergence velocity applied later in the upper mantle at ca. +350 km in

305 horizontal x-direction. Horizontal velocities directly below the mechanical lithosphere (magenta isopleth in fig. 4(f)) indicate that mantle drag in this region forms a zone of locally convergent mantle flow in proximity of the future subduction zone. Conrad and Lithgow-Bertelloni (2002) quantified the importance of slab-pull vs slab-suction force and showed that the slab

pull force and the suction force of a detached slab sinking into the mantle induces similar mantle flow fields. They argued that a detached fraction of a slab sinking into the mantle can exert shear traction forces at the base of the plate and drive the plate. Baes et al. (2018) showed with numerical simulations that sinking of a detached slab below a passive margin can contribute significantly to the initiation of subduction. We argue that the down-welling mantle region observed in M1 and the associated mantle flow also generates a force similar to a slab suction force. To quantify the suction force induced by the down-welling in the convection cell of M1, we calculated the difference of the density in this region with respect to the corresponding initial model density and integrated the density difference spatially over this region. The resulting buoyancy force per unit length is ca. 40 TN m^{-1}, which is in the order of the slab pull force (Turcotte and Schubert, 2014). It is therefore likely that the suction force induced by the convection assists to initiate the subduction and to stabilise the single-slab subduction in simulation M1.

The value of $2 \times \bar{\tau}_{\mathrm{II}}$ is identical to the vertical integral of the difference between the horizontal total stress and the lithostatic pressure, if shear stresses are negligible (Schmalholz et al., 2019). During onset of convergence, when the lithosphere is more or less homogeneously shortened, shear stresses are most likely negligible compared to normal deviatoric stresses. The vertical integral of the difference between the horizontal total stress and the lithostatic pressure represents one of the horizontal driving forces (per unit length) of tectonic plates (Molnar and Lyon-Caen, 1988; Schmalholz et al., 2019). Hence, during convergence before subduction initiation the value of $2 \times \bar{\tau}_{\mathrm{II}}$ represents the plate driving force. In model M1, the maximal value of $2 \times \bar{\tau}_{\mathrm{II}}$ just before stress drop caused by subduction initiation at $\approx$103 Myrs is $\approx$17 TN m^{-1}. However, $2 \times \bar{\tau}_{\mathrm{II}} = \approx 2$ TN m^{-1} at the end of the cooling stage, resulting from stresses due to mantle convection and lateral variation of GPE between continent and basin. Therefore, the $\approx$2 TN m^{-1} can be subtracted from the $\approx$17 TN m^{-1} so that the required plate tectonic driving force for subduction initation is $\approx$15 TN m^{-1} in model M1. Although this value could be further reduced if additional softening mechanisms, such as grain damage or serpentinization during extension, would be considered in the model, we argue that $\approx$15 TN m^{-1} is a feasible value.

Convection is a physical mechanism that can provide additional forces locally to develop and stabilise a single-slab subduction. Double-slab subduction (Holt et al., 2017) is initiated below both of the margins (fig. 6(c)-(e)). These subduction zones are stable only for a short period and the subduction alternates from one margin to the other with ongoing convergence. The resulting slab geometries resemble a symmetric push-down, rather than a stable asymmetric subduction in M2-5. This impacts the deformation in the lithosphere, especially in the crust: the crustal layers of both plates are strongly folded (see fig. 7(b)-(e)). In M1, the deformation of the crustal layers only occurs in the overriding plate. Folding of the crustal layers might be the reason why values of $2 \times \bar{\tau}_{\mathrm{II}}$ increases again after subduction initiation. Although folding is a structural softening mechanism (e.g. Schmalholz et al., 2005; Schmalholz and Mancktelow, 2016), when the folds become more and more isoclinal, the stresses in the crust can be transmitted and are built up again. We, therefore, also stopped the simulations once the crustal folds were essentially isoclinal, because crustal deformation becomes unrealistic. The slightly higher temperatures induced by the effective conductivity reduce the stresses which in turn might explain the lower values of $2 \times \bar{\tau}_{\mathrm{II}}$ compared to values obtained for M1. Also, the higher viscosity limits of M3 and M5 increase the stresses which results in higher values of $2 \times \bar{\tau}_{\mathrm{II}}$ compared to M1. These observations indicate that the effective conductivity approach and high viscosity limits do not only impact the style of subduction, but also impact on the style of deformation in the crust during convergence

The onset of convergence in the simulations has a strong impact on the convection, which can be observed in the change of the velocity field between 99 and 118 Myrs in M1 (see fig. 9(b and c)). Not only the subducting slab may be responsible

345 for changing the convection dynamics, but also the relative horizontal motion of the lithosphere in general. The shear stress induced by the plate movement leads to the decay of the amplitude of these convection cells (e.g. Richter, 1973). Richter (1973) showed analytically that the temporal stability of transversal Rayleigh-Bénard convection cells underneath a moving plate is below 200 Myrs when plate velocities are larger than 2 cm yr^{-1}. Three dimensional numerical simulations showed that Rayleigh-Bénard convection cells with axis parallel to the plate motion are stable below a moving plate (Ballmer et al.,

350 2007), but do, of course, not exist in our 2D models.

4.4 Applications

To apply our models to geodynamic processes on Earth, we compare several model quantities with measurements and indirect estimates of these quantities. The mantle density structure of our model is in good agreement with the preliminary reference Earth model (PREM Dziewonski and Anderson (1981), see fig. 5(b),(e)). The geotherm of the conduction dominated regime

355 lies well in the range of pressure-temperature (P-T) estimates from mantle xenolith data and the geotherm of the convection dominated regime falls within the realistic range for adiabatic gradients and potential mantle temperatures (Hasterok and Chapman (2011), see fig. 5(a),(d)). The heat flux at the base of the lithosphere is in a realistic range of 20-30 mW m^{-2}. The viscosity profiles lie within the range of estimates inferred by inversion of observable geophysical data and from experimentally determined flow law parameters of olivine rheology (Mitrovica and Forte (2004); Behn et al. (2004); Hirth and Kohlstedt (2003),

360 see fig. 5(c),(f)). The lithosphere and mantle velocities are in a realistic range of several cm/yr. The first order lithosphere geometry of the modelled hyper-extended margins and the geometry of the subduction zone seem realistic.

Our model can be applied to some first-order geodynamic processes that were likely important for the orogeny of the Alps. Rifting in the Early to Middle Jurassic (Favre and Stampfli, 1992; Froitzheim and Manatschal, 1996; Handy et al., 2010) lead to the formation of the Piemont-Liguria ocean which was bounded by the hyper-extended magma-poor rifted margins of

365 the Adriatic plate and the Briançonnais domain on the side of the European plate. We follow here the interpretation that the Piemont-Liguria ocean was an embryonic ocean which formed during ultra-slow spreading and was dominated by exhumed subcontinental mantle (e.g. Picazo et al., 2016; McCarthy et al., 2018; Chenin et al., 2019). If true, there was no stable mid-ocean ridge producing a several 100 km wide ocean with a typically 8 km thick oceanic crust and our model would be applicable to the formation of an embryonic ocean with exhumed mantle bounded by magma-poor hyper-extended passive marings. Our

370 models show the formation of a basin with exhumed mantle bounded by hyper-extended margins above a convecting mantle. Hence, our model may describe the first-order thermo-mechanical processes during formation of an embryonic ocean. During closure of the Piemont-Liguria ocean, remnants of those magma-poor ocean-continent transitions escaped subduction and are preserved in the Eastern Alps (Manatschal and Müntener, 2009). We follow the interpretation that the initiation and at least the early stages of ocean closure were caused by far-field convergence between the African and European plates (e.g. Handy et al.,

375 2010). We further assume that subduction was induced, or forced, by this convergence and was not initiated spontaneously due to buoyancy of a cold oceanic lithosphere (De Graciansky et al., 2010). Our models show that a cooling exhumed mantle does

not subduct spontaneously because buoyancy forces are not significant enough to overcome the strength of the lithosphere. However, the models show that convergence of the basin generates a forced subduction initiation at the hyper-extended passive margin causing subduction of the exhumed mantle below the passive margin. Such subduction initiation at the passive margin

380   agrees with geological reconstructions which suggest that the Alpine subduction initiated at the hyper-extended margin of Adria (e.g. Manzotti et al., 2014) and not, for example, within the ocean. Overall, the modelled, more than 100 Myrs long, geodynamic cycle of (1) lithosphere extension generating hyper-extended passive margins and a basin with exhumed mantle, (2) lithosphere cooling for 70 Myrs without spontaneous subduction initiation and (3) convergence leading to forced subduction initiation at one of the hyper-extended margins is in agreement with several geological reconstructions of the Alpine orogeny.

385   However, the Alpine orogeny exhibits a distinct three-dimensional evolution including major stages of strike-slip deformation and a considerably radial shortening direction so that any 2D model can always only address the fundamental aspects of the involved geodynamic processes.

During convergence, several of our models show the formation of a divergent double-slab subduction. Such divergent double-slab subduction likely applies to the Eastward and Westward dipping subduction of the Adriatic plate (Faccenna and Becker,

390   2010; Hua et al., 2017). Another example of divergent double-slab subduction is presumably the Paleo-Asian Ocean, which has been subducted beneath both the southern Siberian Craton in the north and the northern margin of the North China Craton in the south during the Paleozoic (Yang et al., 2017). Furthermore, a divergent double-slab subduction was also suggested between the North Qiangtang and South Qiangtang terrane (Li et al., 2020; Zhao et al., 2015). Our models show that a divergent double-slab subduction is a thermo-mechanically feasible process during convergence of tectonic plates.

395   Tomographic images from the Mediterranean show large p-wave anomalies in the transition zone (Piromallo and Morelli, 2003) indicating that the 660 km phase transition inhibits the sinking material to penetrate further into the lower mantle. This observation suggests that convection in the Alpine-Mediterranean region could be two-layered. Also, mantle convection seems active and largely confined to the upper region of the upper mantle. The convective patterns simulated in our study are in agreement with these observations. We speculate that upper mantle convection might have played a role in the formation of

400   the Alpine orogeny in the form of inducing an additional suction force below the Adriatic margin and assisting the onset of subduction.

4.5   Modelling geodynamic cycles and structural inheritance

We modelled here a geodynamic cycle of subsequent lithosphere hyper-extension with mantle exhumation, thermal relaxation and convergence inducing subduction, all coupled to upper mantle convection, because we wanted to test whether a single and

405   continuous numerical simulation can generate the first order features of these different processes. As we discuss above, our simulation captures the fundamental features of such cycle with model quantities that are applicable to Earth. We argue that the ability of a numerical algorithm with a specific model configuration to generate several geodynamic processes with results applicable to Earth provides further confidence that the model has captured correctly the first order physics of the investigated processes.

410   Geodynamic processes, such as lithosphere extension or convergence, are frequently studied separately. For example, sub-
duction initation at a passive margin during convergence can be studied without a previous extension and cooling stage. An
initial passive margin geometry and thermal field must be then constructed ad-hoc for the model configuration. However, it is
then uncertain whether the applied model would have generated such a margin geometry and thermal structure during an exten-
sion simulation. In other words, it is uncertain whether the initial margin configuration is consistent with the applied model. We

415 modelled here passive margin formation and thermal relaxation before modelling convergence, because we wanted to model
convergence for a passive margin geometry and thermal structure that arises in a self-consistent manner from the applied algo-
rithm and model parameters. Compared to ad-hoc passive margin geometries and temperatures, our modelled margin geometry
is much more heterogeneous. This heterogeneity, or structural inheritance, may have an impact on the subduction initiation. For
example, Kiss et al. (2020) modelled thermal softening induced subduction initiation during convergence of a passive margin,

420 whose geometry and thermal structure was generated ad-hoc as initial model configuration. Their initial passive margin struc-
ture was significantly less heterogeneous than ours. Their model is not directly comparable with ours, because they considered,
amongst others, a homogeneous and not a layered crust and not identical model parameters. However, they applied the same
numerical algorithm. To initiate subduction, they needed a driving force of ≈ 37 TN m^{-1} which is significantly larger than the
≈ 15 TN m^{-1} required in our model M1. We argue that the larger the mechanical, geometrical and thermal heterogeneities

425 are, the smaller may be the required driving force to model subduction initiation by thermal softening. Structural inheritance,
in the form of mechanical and geometrical heterogeneities, cause stress concentrations that can act as trigger for strain local-
ization and shear zone formation. We speculate that even more heterogeneous models with higher numerical resolution than
ours would require even less driving force than ≈ 15 TN m^{-1} to initiate subduction by thermal softening. This is relevant,
because the main argument against thermal softening as an important localization mechanism during lithosphere strain lo-

430 calization and subduction initiation is commonly that the required stresses, and hence driving forces, are too high. In nature,
more softening mechanisms act in concert with thermal softening, such as grain damage (e.g. Bercovici and Ricard, 2012),
fabric and anisotropy evolution (e.g. Montési, 2013) or reaction-induced softening (e.g. White and Knipe, 1978). Including
such additional processes in our mantle-scale numerical models means to include more parameterizations based on not well
constrained parameters and to make more assumptions concerning the up-scaling of such pore- and mineral-scale processes to

435 the applied numerical resolution adapted to the lithosphere and mantle scale. We, therefore, argue that our model is simple but
applicable to first-order processes of lithosphere hyper-extension, upper mantle convection and induced subduction initiation;
and is a starting algorithm for further elaboration with upscaled micro-scale processes.

5   Conclusions

Our 2D thermo-mechanical numerical model of coupled lithosphere-mantle deformation is able to generate a 120 Myrs long

440 geodynamic cycle of subsequent extension (30 Myrs), cooling (70 Myrs) and convergence (20 Myrs) in a single and contin-
uous simulation. During lithosphere extension, our models generate an approximately 400 km wide basin of exhumed mantle
bounded by hyper-extended magma-poor passive margins. Physical fields, such as temperature, density and viscosity structure

produced by our models are in good agreement with petrological data, data inferred from geophysical observable quantities and from laboratory experiments. The models show that considering only the thermal effects of upper mantle convection by

445 using an effective thermal conductivity generates results of lithosphere hyper-extension that are similar to the ones of models that explicitly model the convective flow. The inferred viscosity structure in the mantle, parameterized by different effective viscosity cut-offs has a significant impact on the simulation results. After 70 Myrs of cooling without far-field deformation, subduction of the exhumed and cold mantle was not spontaneously initiated. The density difference between lithosphere and underlying mantle is too small to generate a downward pulling buoyancy force that can exceed the mechanical strength of

450 the cold lithosphere. The modelled extension and cooling stages generate a structural and thermal inheritance, in the form of mechanical, geometrical and thermal heterogeneities, in a self-consistent way for the subsequent convergence stage. Convergence of the basin initiates subduction of the exhumed mantle at the transition to the hyper-extended margins. The main mechanism of strain localization causing subduction initiation is thermal softening. If convection in the mantle is suppressed by high effective thermal conductivities or high, lower viscosity limits, then subduction initiates at both margins leading to

455 divergent double-slab subduction. Thermal convection in the mantle assists to generate a single-slab subduction at only one margin, likely due to mantle flow which exerts an additional suction force on the lithosphere. Subduction is initiated during convergence for plate driving forces of approximately 15 TN m^{-1}. Overall, our models suggest that upper mantle convection can have a considerable impact on lithosphere deformation, mainly due to mantle flow and associated suction forces.

For conditions applicable to Earth, our models generate the first-order, large-scale features of hyper-extension and subduc-

460 tion initiation. On the crustal and lithospheric scales, structural softening, due to non-linear flow laws and mechanical heterogeneities, and thermal softening, due to energy conservation and temperature-dependent viscosities, are softening mechanisms that are sufficient to generate these first-order features. We, hence, argue that these two softening mechanisms are important for lithosphere deformation.

Our models are also useful to test mantle flow laws, or flow law parameters, because flow laws generating too low effective

465 viscosities, in our case for wet olivine, generate too vigorous convection associated with an unrealistic thermal erosion of the lithosphere.

The first-order geodynamic processes simulated in the geodynamic cycle of subsequent extension, cooling and convergence are applicable to orogenies that resulted from the opening and closure of embryonic oceans, which might have been the case for the Alpine orogeny.

470 *Data availability.* The data presented in this study are available on request from Lorenzo G. Candioti.

Appendix A: Numerical algorithm

The applied algorithm has already been used to model processes at different scales, such as deformation of eclogites on the centimetre-scale (Yamato et al., 2019), crystal-melt segregation of magma during its ascent in a meter-scale conduit (Yamato

et al., 2015), rifting of continental lithosphere (Duretz et al., 2016b; Petri et al., 2019), stress calculations around the Tibetan
475 Plateau (Schmalholz et al., 2019) and within and around a subduction of an oceanic plate (Bessat et al., 2020), as well as
modelling Precambrian orogenic processes (Poh et al., 2020).

Continuity and force balance equations for an incompressible slowly flowing (no inertial forces) fluid under gravity are given
by

$$\frac{\partial v_i}{\partial x_i} = 0 \tag{A1}$$

$$480 \quad \frac{\partial \sigma_{ij}}{\partial x_j} = -\rho\, \boldsymbol{a}_i \,, \tag{A2}$$

where v_i denotes velocity vector components and x_i spatial coordinate components, where (i,j=1) indicates the horizontal
direction and (i,j=2) the vertical direction, σ_{ij} are components of the total stress tensor, ρ is density and $\boldsymbol{a}_i = [0; g]$ is a vector
with g being the gravitational acceleration. Density is a function of pressure P (negative mean stress) and temperature T
computed as a simplified equation of state for the crustal phases like

$$485 \quad \rho(P,T) = \rho_0 \left(1 - \alpha\Delta T\right)\left(1 + \beta\Delta P\right) \,, \tag{A3}$$

where ρ_0 is the material density at the reference temperature T_0 and pressure P_0, $\Delta T = T - T_0$ and $\Delta P = P - P_0$. Effective
density for the mantle phases is pre-computed using the software package Perple_X (Connolly, 2005) for the bulk rock compo-
sition of a Hawaiian pyrolite (Workman and Hart, 2005). Figure A1 shows the density distribution for the calculated pressure
and temperature range.

490 The viscoelastic stress tensor components are defined using a backward-Euler scheme (e.g., Schmalholz et al., 2001) as

$$\sigma_{ij} = -P\delta_{ij} + 2\left(\frac{1}{\eta^{\mathrm{eff}}} + \frac{1}{G\Delta t}\right)^{-1} \dot{\varepsilon}_{ij} + \left(1 + \frac{G\Delta t}{\eta^{\mathrm{eff}}}\right)^{-1} \tau_{ij}^o + J_{ij} \,, \tag{A4}$$

where $\delta_{ij} = 0$ if $i \neq j$, or $\delta_{ij} = 1$ if $i = j$, η^{eff} is the effective viscosity, G is shear modulus, Δt is the time step, $\dot{\varepsilon}_{ij}$ are the
components of the deviatoric strain rate tensor, τ_{ij}^o is the deviatoric stress tensor of the preceding time step and J_{ij} comprises
components of the Jaumann stress rate as described in detail in Beuchert and Podladchikov (2010). A visco-elasto-plastic
495 Maxwell model is used to describe the rheology, implying that the components of the total deviatoric strain rate tensor $\dot{\varepsilon}_{ij}$
are additively decomposed into contributions from the viscous (dislocation, diffusion and Peierls creep), plastic and elastic
deformation as

$$\dot{\varepsilon}_{ij} = \dot{\varepsilon}_{ij}^{\mathrm{ela}} + \dot{\varepsilon}_{ij}^{\mathrm{pla}} + \dot{\varepsilon}_{ij}^{\mathrm{dis}} + \dot{\varepsilon}_{ij}^{\mathrm{dif}} + \dot{\varepsilon}_{ij}^{\mathrm{pei}} \,, \tag{A5}$$

A local iteration cycle is performed on each cell/node until eq. A5 is satisfied (e.g., Popov and Sobolev, 2008). The effective
viscosity for the dislocation and Peierls creep flow law is a function of the second invariant of the respective strain rate
components $\dot{\varepsilon}_{\mathrm{II}}^{\mathrm{dis,pei}} = \tau_{\mathrm{II}}/(2\eta^{\mathrm{dis,pei}})$

$$\eta^{\mathrm{dis}} = \frac{2^{\frac{1-n}{n}}}{3^{\frac{1+n}{2n}}} A^{-1} \left(\dot{\varepsilon}_{\mathrm{II}}^{\mathrm{dis}}\right)^{\frac{1}{n}-1} \exp\left(\frac{Q+PV}{nRT}\right) \left(f_{\mathrm{H_2O}}\right)^{-\frac{r}{n}}, \tag{A6}$$

where the ratio in front of the pre-factor A results from conversion of the experimentally derived 1D flow law, obtained from
laboratory experiments, to a flow law for tensor components (e.g., Schmalholz and Fletcher, 2011). For the mantle material
diffusion creep is taken into account and its viscosity takes the following form

$$\eta^{\mathrm{dif}} = \frac{1}{3} A^{-1} d^m \exp\left(\frac{Q+PV}{RT}\right) \left(f_{\mathrm{H_2O}}\right)^{-r}, \tag{A7}$$

where d is grain size and m is a grain size exponent. Effective Peierls viscosity is calculated using the regularised form of
Kameyama et al. (1999) for the experimentally derived flow law by Goetze and Evans (1979) as

$$\eta^{\mathrm{pei}} = \frac{2^{\frac{1-s}{s}}}{3^{\frac{1+s}{2s}}} \hat{A} \left(\dot{\varepsilon}_{\mathrm{II}}^{\mathrm{pei}}\right)^{\frac{1}{s}-1}, \tag{A8}$$

where s is an effective, temperature dependent stress exponent:

$$s = 2\,\gamma\,\frac{Q}{RT}\left(1-\gamma\right). \tag{A9}$$

$\hat{A}$ in Eq. (A8) is

$$\hat{A} = \left[A_{\mathrm{P}} \exp\left(-\frac{Q(1-\gamma)^2}{RT}\right)\right]^{-\frac{1}{s}} \gamma\sigma_{\mathrm{P}}, \tag{A10}$$

where γ is a fitting parameter. In the frictional domain, stresses are limited by a yield stress τ_{y} obtained by a Drucker-Prager
yield criterion

$$\tau_{\mathrm{y}} = P\,\sin\phi + C\,\cos\phi, \tag{A11}$$

where ϕ is the internal angle of friction and C is the cohesion. If the yield condition is met ($f = \tau_{\mathrm{II}} - \tau_{\mathrm{y}} > 0$) the equivalent
plastic viscosity is computed as

$$\eta^{\mathrm{pla}} = \frac{\tau_{\mathrm{y}}}{2\dot{\varepsilon}_{\mathrm{II}}^{\mathrm{pla}}}, \tag{A12}$$

520   At the end of the iteration cycle, the effective viscosity in eq. A4 is computed as the inverse of the quasi-harmonic average of the viscous and the plastic contributions for the corresponding invariants of the strain rate tensor components of the distinct deformation mechanisms as

$$\eta^{\text{eff}} = \left(\frac{1}{\eta^{\text{dis}}} + \frac{1}{\eta^{\text{dif}}} + \frac{1}{\eta^{\text{pei}}} + \frac{1}{\eta^{\text{pla}}} \right)^{-1} . \tag{A13}$$

Thermal evolution of the model is calculated with the heat transfer equation

525     $$\rho \, c_{\text{P}} \, \frac{\text{D}T}{\text{D}t} = \frac{\partial}{\partial x_i} \left(k_{\text{th}} \, \frac{\partial T}{\partial x_i} \right) + H_{\text{A}} + H_{\text{D}} + H_{\text{R}} \, , \tag{A14}$$

where c_P is the specific heat capacity at constant pressure, $\text{D}/\text{D}t$ is the material time derivative, k_{th} is thermal conductivity, $H_{\text{A}} = T \alpha v_z g \rho$ is a heat source or sink resulting from adiabatic processes assuming lithostatic pressure conditions, $H_{\text{D}} = \tau_{ij}^2 / \left(2\eta^{\text{eff}} \right)$ results from the conversion of dissipative work into heat (so-called shear heating) and H_{R} is a radiogenic heat source. All physical parameters are summarised in table 2.

530   **Appendix B: Nusselt number scaling laws and phase transitions**

Modelling thermal convection beneath an actively deforming lithosphere can be numerically expensive, because the convection velocities can be as high as or even higher than the motion of the lithospheric plates, depending on the vigour of the convecting system. This significantly reduces the maximum time step necessary to ensure numerical stability. In consequence, it takes more time steps to run a simulation to the same physical time when convection is modelled together with deformation in the
535 lithosphere. Hence, the computational time can be twice as long compared to models, where only the deforming lithosphere is modelled. However, it is possible to include the effect of thermal convection in the mantle and keep a constant vertical heat flux through the lithosphere-asthenosphere boundary (LAB) into a numerical model without explicitly modelling convection by using an effective thermal conductivity for the mantle material below the lithosphere. Two dimensionless quantities have to be defined, namely the Rayleigh and Nusselt numbers. The Rayleigh number is the ratio of the thermal diffusion and advection
540 time scale

$$Ra = \frac{\rho g \alpha \Delta T D^3}{\kappa \eta_{\text{eff}}} \, , \tag{B1}$$

where ρ is density, g is gravitational acceleration, α is a coefficient of thermal expansion, ΔT is the temperature difference between the top and the bottom and D is the thickness of the convecting layer, $\kappa = k_{\text{th}} / \rho / c_P$ is the thermal diffusivity and η_{eff} is the effective viscosity. The Nusselt number can be expressed in terms of the Rayleigh number as

545   $$Nu = \left(\frac{Ra}{Ra_{\text{crit}}} \right)^{\beta} , \tag{B2}$$

where Ra_{crit} is the critical Rayleigh number, typical in the order of 10^3, at which convection starts and β is a power-law exponent (Schubert et al., 2001). The Nusselt number is the ratio of advective heat flux, q_{adv}, which is the vertical heat flux through the base of the lithosphere, q_{LAB}, imposed by the convecting upper mantle to the diffusive heat flux, q_{dif}, imposed by the lithosphere on top of the convecting upper mantle as

550
$$Nu = \frac{q_{\mathrm{Adv}}}{q_{\mathrm{Dif}}} = \frac{q_{\mathrm{LAB}}}{\frac{k_{\mathrm{th}}(T_{\mathrm{M}}-T_{\mathrm{LAB}})}{D}} \; , \qquad (B3)$$

where k_{th} is thermal conductivity, T_{M} is the average temperature of the upper mantle and T_{LAB} is the temperature at the base of the lithosphere. Using this relationship, it is possible to scale the thermal conductivity to the Nusselt number of the Earth's mantle and to maintain a constant heat flow through the base of the lithosphere via conduction when convection is absent. Assuming a vertical heat flow of $30\ \mathrm{mW\ m^{-2}}$ through the base of the lithosphere, $Ra = 2 \times 10^6$ and $\beta = 1/3$ for the Earth's

555 upper mantle convection, eq. B2 predicts $Nu = 13$. This implies that the heat flow provided by advection is $13\times$ higher than the heat flow provided by conduction. Equation B3 allows for three possibilities to balance the excess advective heat flow through the lithosphere: (1) D can be reduced by a factor 13, (2) $(T_{\mathrm{M}}-T_{\mathrm{LAB}})$ or (3) k_{th} can be increased by a factor 13. Since it is desired to mimic the convection in the upper mantle down to a depth of 660 km, neither D nor $(T_{\mathrm{M}}-T_{\mathrm{LAB}})$ can be changed. Hence, k_{th} of the asthenosphere needs to be $13\times$ higher than the realistic value to balance the heat flow through the lithosphere by

560 conduction only. For this study, the realistic value for $k_{\mathrm{th}} = 2.75$ and $k_{\mathrm{eff}} = 36$. Calculating the effective conductive heat flow through the base of the lithosphere q_{eff}

$$q_{\mathrm{eff}} = k_{\mathrm{eff}} \frac{T_{\mathrm{LAB}} - T_{\mathrm{bot}}}{D} \qquad (B4)$$

using $T_{\mathrm{LAB}} = 1350\ ^{\circ}\mathrm{C}$ and $T_{\mathrm{bot}} = 1612\ ^{\circ}\mathrm{C}$ as temperatures at the LAB and at a depth of 660 km and a total depth of the upper mantle and transition zone of 540 km yields a vertical heat flow $q_{\mathrm{eff}} = 32\ \mathrm{mW\ m^2}$, which is consistent with the mean

565 heat flow at the base of continental lithosphere (Turcotte and Schubert, 2014). To avoid a strong contrast of conductivities directly at the base of the lithosphere we linearly increase the conductivity from 2.75-36 $\mathrm{W\ m^{-1}\ K^{-1}}$ over a temperature range of 1350-1376 $^{\circ}\mathrm{C}$.

As mentioned above, the vigour of convection is defined by the Rayleigh number (eq. B1). For $Ra > Ra_{\mathrm{crit}}$, the time scale for thermal diffusion is much larger than the time scale for advection of material. This means that the entropy of the system

570 remains relatively constant in time. By definition, such a system is adiabatic (Kondepudi and Prigogine, 2014). In the presented simulations, the density and entropy for the mantle phases is pre-computed using Perple_X for a given bulk rock composition. Assuming that the temperature gradient in the upper mantle is adiabatic and stress conditions are close to lithostatic (i.e., deviatoric stresses are negligible), the temperature at any depth can be determined by following an isentrop from the Perple_X database. Starting coordinates in pressure-temperature space are the (lithostatic) conditions at the base of the lithosphere. From

575 these pressure and temperature values one can follow the closest isentrop (black line Fig. A1) until the (lithostatic) pressure value at target depth (in this study 660 km, red diamond Fig. A1) is reached and extract the corresponding temperature value.

Trubitsyn and Trubitsyna (2015) derived an analytical solution to calculate temperatures assuming an adiabatic gradient for given depths. We determined the temperature at the bottom of the model domain using both approaches and the obtained values that differ by only 0.01 °C. We use an extended Boussinesq approximation, which means that terms describing adiabatic
580 processes only appear in eq. A14 (Petersen et al., 2010), density variations due to temperature gradients are negligible on the long term, but temperature changes due to adiabatic processes can be as high as the contribution of radiogenic heat production in the mantle. Boundary conditions at the bottom of the domain are set to free slip, that is the vertical velocity is zero. This represents an impermeable mechanical boundary that mimics the phase transition of γ-spinel olivine to Mg-Perovskite at pressure and temperature conditions at a depth of 660 km and we here assume that convection in the mantle is two-layered.

585 **Appendix C: Convection benchmark**

In this section, we present the results of a convection benchmark performed by the algorithm used in this study. Equations for continuity and force balance are solved as in eq. A1 and A2, density is a function of temperature only and calculated as

$$\rho(T) = \rho_0(1 - \alpha T) \tag{C1}$$

and the total stress tensor is decomposed into a pressure and a deviatoric part as

590 $$\sigma_{ij} = -P\delta_{ij} + \tau_{ij} . \tag{C2}$$

Transfer of heat is calculated as in eq.A14. Stresses and strain rates ($\dot{\varepsilon}_{ij}$) are related to each other via the viscosity η as

$$\tau_{ij} = 2\eta\dot{\varepsilon}_{ij} . \tag{C3}$$

Viscosity is computed via a linearized Arrhenius law, also called Frank-Kamenetskii approximation (Kamenetskii, 1969):

$$\eta(T,z) = \exp(-\gamma_T + \gamma_z) , \tag{C4}$$

595 with $\gamma_T = \log(\eta_T)$ and $\gamma_z = \log(\eta_z)$. By choosing $\eta_z = 1$, $\gamma_z = 0$ in eq. C4 and, therefore, the viscosity is only temperature dependent.

The dimensionless equations are discretized over a domain that extends from 0 to 1 in both horizontal and vertical directions and a small amplitude perturbation is applied to the initial temperature profile as

$$T(x,z) = (1-z) + A\cos(\pi x)\sin(\pi z) . \tag{C5}$$

600   As mentioned above, the vigour of the convecting system is described by its Rayleigh number (eq. B1). A local $Ra = 10^2$ is applied to the top boundary by setting $\alpha = 10^{-2}$, $g = 10^4$ and all other parameters of eq.B1 are set to 1. The applied viscosity decrease by choosing $\eta_T = 10^5$ in eq. C4 results in a global $Ra = 10^7$. All mechanical boundaries are set to free slip, the thermal boundary conditions are constant temperature at the top ($T = 0$) and bottom ($T = 1$) and insulating (i.e., zero flux) at the two vertical boundaries. Tosi et al. (2015) tested several algorithms, including finite element, finite differences, finite volume and

605   spectral discretization, on their capability of modelling distinct rheologies of the mantle, from temperature dependent viscosity only up to visco-plastic rheologies. We have chosen the simplest test, case one in Tosi et al. (2015), and report the results of two distinct diagnostic quantities: the average temperature over the entire modelling domain

$$\langle T \rangle = \int\limits_0^1 \int\limits_0^1 T \,\mathrm{dx}\mathrm{dz} \tag{C6}$$

and the root mean square velocity at the surface

610    $$u_{\mathrm{RMS}}^{\mathrm{surf}} = \left(\int\limits_0^1 v_x^2 \Big|_{z=1} \,\mathrm{dx} \right)^{\frac{1}{2}}. \tag{C7}$$

The model develops one convection cell below a stagnant lid (fig.A2(a), (b)). Diagnostic quantities of average temperature (fig.A2(c)) and root-mean square velocity (fig.A2(d)) at the top of the domain agree with values that have been produced by the algorithms (grey areas in fig.A2(c) and (d)) tested in Tosi et al. (2015). We tested numerical resolutions of 50^2, 100^2, 150^2 and 300^2. Only for resolutions $>100^2$ the desired convective pattern developed. The numerical algorithms tested by Tosi et al.

615   (2015) passed the benchmark already for lower resolutions. This is due to the fact that the algorithm presented here uses a uniform grid size across the domain. The algorithms tested by Tosi et al. (2015) used refined meshes. Sufficient resolution of the thermal boundary layers at the top and at the bottom is crucial to develop the desired pattern. Using a refined mesh in these regions, allows for lower total resolution, whereas using a regular mesh necessitates a much higher resolution in total. Nevertheless, values for the diagnostic quantities reproduced by the presented algorithm lie well within the minimum and

620   maximum values calculated by the algorithms tested in Tosi et al. (2015) (grey areas in fig. A2(b) & (c)). This shows that the convection in the upper mantle, where the viscosity is essentially temperature dependent, in the simulations presented in this study in which convection is not parameterized, is accurately modelled.

Appendix D: Gravitational potential energy and plate driving forces

We use the gravitational potential energy per unit surface (*GPE*) to quantify the impact of convection induced density variations
625 in the upper mantle during the distinct stages of the simulations. The *GPE* varies along the horizontal x-direction and is computed as

$$GPE(x) = \int_{Sb}^{St(x)} P_{\mathrm{L}}(x,z)\ \mathrm{d}z, \tag{D1}$$

where P_{L} is the lithostatic pressure calculated as

$$P_{\mathrm{L}}(x,z) = \int_{z}^{St(x)} \rho(x,z')\ g\ \mathrm{d}z' \tag{D2}$$

630 and $St(x)$ is the stress-free surface and Sb is the model bottom. Horizontal variations in *GPE*, ΔGPE, are calculated by subtracting the leftmost value as a reference value from all other values. The *GPE* gives an estimate on the plate driving forces per unit length (Molnar and Lyon-Caen, 1988; Schmalholz et al., 2019; Bessat et al., 2020) acting in the system during the different stages of the hyper-extension and convergence cycle. We also calculate the vertical integral of the second invariant of the deviatoric stress tensor

635
$$\bar{\tau}_{\mathrm{II}}(x) = \int_{Sb}^{St(x)} \tau_{\mathrm{II}}(x,z)\ \mathrm{d}z \tag{D3}$$

which also can be used to estimate the plate driving force (see fig.8(d)). For calculation of the suction force per unit length induced by the mantle flow in fig. 4(a) & (f) we used the following formula

$$F = \int_{b}^{a} \int_{d}^{c} \Delta \rho g\ \mathrm{d}z\ \mathrm{d}x\ , \tag{D4}$$

where $a = 350$ km, $b = 150$ km, $c = -120$ km and $d = -450$ km are the integration bounds and $\Delta \rho$ is the difference in
640 density between the initial density field and the density field at the end of the thermal relaxation period.

Author contributions. Lorenzo G. Candioti configured and performed the numerical simulations and the convection benchmark, interpreted the numerical results, generated the figures and wrote the manuscript. Stefan M. Schmalholz designed the numerical study, helped in interpreting the results and designing the figures and contributed to writing the manuscript. Thibault Duretz developed the applied numerical algorithm and helped in configuring the model and the interpretation of the results.

645 *Competing interests.* The authors declare that they have no conflict of interest.

Acknowledgements. This work is supported by SNF grant No. 200020 163169. Scientific colour maps used in all figures are taken from Crameri (2018).

References

Afonso, J., Ranalli, G., and Fernandez, M.: Density structure and buoyancy of the oceanic lithosphere revisited, Geophysical Research
650   Letters, 34, 2007.

Baes, M., Sobolev, S. V., and Quinteros, J.: Subduction initiation in mid-ocean induced by mantle suction flow, Geophysical Journal International, 215, 1515–1522, 2018.

Ballmer, M., Van Hunen, J., Ito, G., Tackley, P., and Bianco, T.: Non-hotspot volcano chains originating from small-scale sublithospheric convection, Geophysical Research Letters, 34, 2007.

655 Beaussier, S. J., Gerya, T. V., and Burg, J.-P.: 3D numerical modelling of the Wilson cycle: structural inheritance of alternating subduction polarity, Geological Society, London, Special Publications, 470, 439–461, 2019.

Becker, T. W.: Superweak asthenosphere in light of upper mantle seismic anisotropy, Geochemistry, Geophysics, Geosystems, 18, 1986–2003, 2017.

Behn, M. D., Conrad, C. P., and Silver, P. G.: Detection of upper mantle flow associated with the African Superplume, Earth and Planetary
660   Science Letters, 224, 259–274, 2004.

Bercovici, D. and Ricard, Y.: Mechanisms for the generation of plate tectonics by two-phase grain-damage and pinning, Physics of the Earth and Planetary Interiors, 202, 27–55, 2012.

Bessat, A., Duretz, T., Hetényi, G., Pilet, S., and Schmalholz, S. M.: Stress and deformation mechanisms at a subduction zone: insights from 2D thermo-mechanical numerical modelling, Geophysical Journal International, 2020.

665 Beuchert, M. J. and Podladchikov, Y. Y.: Viscoelastic mantle convection and lithospheric stresses, geophysical Journal international, 183, 35–63, 2010.

Boonma, K., Kumar, A., García-Castellanos, D., Jiménez-Munt, I., and Fernández, M.: Lithospheric mantle buoyancy: the role of tectonic convergence and mantle composition, Scientific Reports, 9, 1–8, 2019.

Brune, S., Williams, S. E., Butterworth, N. P., and Müller, R. D.: Abrupt plate accelerations shape rifted continental margins, Nature, 536,
670   201–204, 2016.

Chenin, P., Manatschal, G., Picazo, S., Müntener, O., Karner, G., Johnson, C., and Ulrich, M.: Influence of the architecture of magma-poor hyperextended rifted margins on orogens produced by the closure of narrow versus wide oceans, Geosphere, 13, 559–576, 2017.

Chenin, P., Picazo, S., Jammes, S., Manatschal, G., Müntener, O., and Karner, G.: Potential role of lithospheric mantle composition in the Wilson cycle: a North Atlantic perspective, Geological Society, London, Special Publications, 470, 157–172, 2019.

675 Cloos, M.: Lithospheric buoyancy and collisional orogenesis: Subduction of oceanic plateaus, continental margins, island arcs, spreading ridges, and seamounts, Geological Society of America Bulletin, 105, 715–737, 1993.

Connolly, J. A.: Computation of phase equilibria by linear programming: a tool for geodynamic modeling and its application to subduction zone decarbonation, Earth and Planetary Science Letters, 236, 524–541, 2005.

Conrad, C. P. and Lithgow-Bertelloni, C.: How mantle slabs drive plate tectonics, Science, 298, 207–209, 2002.

680 Crameri, F.: Geodynamic diagnostics, scientific visualisation and StagLab 3.0, Geoscientific Model Development, 11, 2541–2562, 2018.

Crameri, F., Conrad, C. P., Montési, L., and Lithgow-Bertelloni, C. R.: The dynamic life of an oceanic plate, Tectonophysics, 760, 107–135, 2019.

Currie, C. A., Huismans, R. S., and Beaumont, C.: Thinning of continental backarc lithosphere by flow-induced gravitational instability, Earth and Planetary Science Letters, 269, 436–447, 2008.

685 Dal Zilio, L., Faccenda, M., and Capitanio, F.: The role of deep subduction in supercontinent breakup, Tectonophysics, 746, 312–324, 2018.

De Graciansky, P.-C., Roberts, D. G., and Tricart, P.: The Western Alps, from rift to passive margin to orogenic belt: an integrated geoscience overview, Elsevier, 2010.

Duretz, T., May, D. A., and Yamato, P.: A free surface capturing discretization for the staggered grid finite difference scheme, Geophysical Journal International, 204, 1518–1530, 2016a.

690 Duretz, T., Petri, B., Mohn, G., Schmalholz, S., Schenker, F., and Müntener, O.: The importance of structural softening for the evolution and architecture of passive margins, Scientific reports, 6, 38 704, 2016b.

Dziewonski, A. M. and Anderson, D. L.: Preliminary reference Earth model, Physics of the earth and planetary interiors, 25, 297–356, 1981.

England, P., Molnar, P., and Richter, F.: John Perry's neglected critique of Kelvin's age for the Earth: A missed opportunity in geodynamics, GSA Today, 17, 2007.

695 Erdös, Z., Huismans, R., and van der Beek, P.: Control of increased sedimentation on orogenic fold-and-thrust belt structure-insights into the evolution of the Western Alps, 2019.

Faccenna, C. and Becker, T. W.: Shaping mobile belts by small-scale convection, Nature, 465, 602–605, 2010.

Favre, P. and Stampfli, G.: From rifting to passive margin: the examples of the Red Sea, Central Atlantic and Alpine Tethys, Tectonophysics, 215, 69–97, 1992.

700 Forte, A. M., Quéré, S., Moucha, R., Simmons, N. A., Grand, S. P., Mitrovica, J. X., and Rowley, D. B.: Joint seismic–geodynamic-mineral physical modelling of African geodynamics: A reconciliation of deep-mantle convection with surface geophysical constraints, Earth and Planetary Science Letters, 295, 329–341, 2010.

Froitzheim, N. and Manatschal, G.: Kinematics of Jurassic rifting, mantle exhumation, and passive-margin formation in the Austroalpine and Penninic nappes (eastern Switzerland), Geological society of America bulletin, 108, 1120–1133, 1996.

705 Garel, F., Goes, S., Davies, D., Davies, J. H., Kramer, S. C., and Wilson, C. R.: Interaction of subducted slabs with the mantle transition-zone: A regime diagram from 2-D thermo-mechanical models with a mobile trench and an overriding plate, Geochemistry, Geophysics, Geosystems, 15, 1739–1765, 2014.

Gerya, T. V. and Yuen, D. A.: Characteristics-based marker-in-cell method with conservative finite-differences schemes for modeling geological flows with strongly variable transport properties, Physics of the Earth and Planetary Interiors, 140, 293–318, 2003.

710 Goetze, C. and Evans, B.: Stress and temperature in the bending lithosphere as constrained by experimental rock mechanics, Geophysical Journal International, 59, 463–478, 1979.

Golabek, G. J., Keller, T., Gerya, T. V., Zhu, G., Tackley, P. J., and Connolly, J. A.: Origin of the Martian dichotomy and Tharsis from a giant impact causing massive magmatism, Icarus, 215, 346–357, 2011.

Handy, M. R., Schmid, S. M., Bousquet, R., Kissling, E., and Bernoulli, D.: Reconciling plate-tectonic reconstructions of Alpine Tethys with

715 the geological–geophysical record of spreading and subduction in the Alps, Earth-Science Reviews, 102, 121–158, 2010.

Hasterok, D. and Chapman, D.: Heat production and geotherms for the continental lithosphere, Earth and Planetary Science Letters, 307, 59–70, 2011.

Hirth, G. and Kohlstedt, D.: Rheology of the upper mantle and the mantle wedge: A view from the experimentalists, GEOPHYSICAL MONOGRAPH-AMERICAN GEOPHYSICAL UNION, 138, 83–106, 2003.

720 Holt, A., Royden, L., and Becker, T.: The dynamics of double slab subduction, Geophysical Journal International, 209, 250–265, 2017.

Hua, Y., Zhao, D., and Xu, Y.: P wave anisotropic tomography of the Alps, Journal of Geophysical Research: Solid Earth, 122, 4509–4528, 2017.

Huismans, R. and Beaumont, C.: Depth-dependent extension, two-stage breakup and cratonic underplating at rifted margins, Nature, 473, 74–78, 2011.

725   Jammes, S. and Huismans, R. S.: Structural styles of mountain building: Controls of lithospheric rheologic stratification and extensional inheritance, Journal of Geophysical Research: Solid Earth, 117, 2012.

Jaquet, Y. and Schmalholz, S. M.: Spontaneous ductile crustal shear zone formation by thermal softening and related stress, temperature and strain rate evolution, Tectonophysics, 746, 384–397, 2018.

Kamenetskii, D. F.: Diffusion and heat transfer in chemical kinetics, Plenum Press, New York, 1969.

730   Kameyama, M., Yuen, D. A., and Karato, S.-I.: Thermal-mechanical effects of low-temperature plasticity (the Peierls mechanism) on the deformation of a viscoelastic shear zone, Earth and Planetary Science Letters, 168, 159–172, 1999.

Kaus, B. J., Liu, Y., Becker, T., Yuen, D. A., and Shi, Y.: Lithospheric stress-states predicted from long-term tectonic models: Influence of rheology and possible application to Taiwan, Journal of Asian Earth Sciences, 36, 119–134, 2009.

Kiss, D., Candioti, L. G., Duretz, T., and Schmalholz, S. M.: Thermal softening induced subduction initiation at a passive margin, Geophysical
735   Journal International, 220, 2068–2073, 2020.

Kondepudi, D. and Prigogine, I.: Modern thermodynamics: from heat engines to dissipative structures, John Wiley & Sons, 2014.

Kronenberg, A. K., Kirby, S. H., and Pinkston, J.: Basal slip and mechanical anisotropy of biotite, Journal of Geophysical Research: Solid Earth, 95, 19 257–19 278, 1990.

Li, D., Wang, G., Bons, P., Zhao, Z., Du, J., Wang, S., Yuan, G., Liang, X., Zhang, L., Li, C., et al.: Subduction reversal in a divergent double
740   subduction zone drives the exhumation of southern Qiangtang blueschist-bearing mélange, central Tibet, Tectonics, 2020.

Li, Z.-H., Gerya, T., and Connolly, J. A.: Variability of subducting slab morphologies in the mantle transition zone: Insight from petrological-thermomechanical modeling, Earth-Science Reviews, 2019.

Mackwell, S., Zimmerman, M., and Kohlstedt, D.: High-temperature deformation of dry diabase with application to tectonics on Venus, Journal of Geophysical Research: Solid Earth, 103, 975–984, 1998.

745   Manatschal, G. and Müntener, O.: A type sequence across an ancient magma-poor ocean–continent transition: the example of the western Alpine Tethys ophiolites, Tectonophysics, 473, 4–19, 2009.

Manzotti, P., Ballevre, M., Zucali, M., Robyr, M., and Engi, M.: The tectonometamorphic evolution of the Sesia–Dent Blanche nappes (internal Western Alps): review and synthesis, Swiss Journal of Geosciences, 107, 309–336, 2014.

McCarthy, A., Chelle-Michou, C., Müntener, O., Arculus, R., and Blundy, J.: Subduction initiation without magmatism: The case of the
750   missing Alpine magmatic arc, Geology, 46, 1059–1062, 2018.

McKenzie, D.: The initiation of trenches: a finite amplitude instability, Island arcs, deep sea trenches and back-arc basins, 1, 57–61, 1977.

Mitrovica, J. and Forte, A.: A new inference of mantle viscosity based upon joint inversion of convection and glacial isostatic adjustment data, Earth and Planetary Science Letters, 225, 177–189, 2004.

Molnar, P. and Lyon-Caen, H.: Some simple physical aspects of the support, structure, and evolution of mountain belts, Processes in conti-
755   nental lithospheric deformation, 218, 179–207, 1988.

Montési, L. G.: Fabric development as the key for forming ductile shear zones and enabling plate tectonics, Journal of Structural Geology, 50, 254–266, 2013.

Mueller, S. and Phillips, R. J.: On the initiation of subduction, Journal of Geophysical Research: Solid Earth, 96, 651–665, 1991.

Parsons, B. and McKenzie, D.: Mantle convection and the thermal structure of the plates, Journal of Geophysical Research: Solid Earth, 83,
760   4485–4496, 1978.

Peron-Pinvidic, G., Manatschal, G., et al.: Rifted margins: state of the art and future challenges, Frontiers in Earth Science, 7, 218, 2019.

Petersen, K. D., Nielsen, S., Clausen, O., Stephenson, R., and Gerya, T.: Small-scale mantle convection produces stratigraphic sequences in sedimentary basins, Science, 329, 827–830, 2010.

Petri, B., Duretz, T., Mohn, G., Schmalholz, S. M., Karner, G. D., and Müntener, O.: Thinning mechanisms of heterogeneous continental lithosphere, Earth and Planetary Science Letters, 512, 147–162, 2019.

Picazo, S., Müntener, O., Manatschal, G., Bauville, A., Karner, G., and Johnson, C.: Mapping the nature of mantle domains in Western and Central Europe based on clinopyroxene and spinel chemistry: Evidence for mantle modification during an extensional cycle, Lithos, 266, 233–263, 2016.

Piromallo, C. and Morelli, A.: P wave tomography of the mantle under the Alpine-Mediterranean area, Journal of Geophysical Research: Solid Earth, 108, 2003.

Poh, J., Yamato, P., Duretz, T., Gapais, D., and Ledru, P.: Precambrian deformation belts in compressive tectonic regimes: A numerical perspective, Tectonophysics, 777, 228 350, 2020.

Popov, A. and Sobolev, S.: SLIM3D: A tool for three-dimensional thermomechanical modeling of lithospheric deformation with elasto-visco-plastic rheology, Physics of the Earth and Planetary Interiors, 171, 55–75, 2008.

Ranalli, G.: Rheology of the Earth, Springer Science & Business Media, 1995.

Ricard, Y., Vigny, C., and Froidevaux, C.: Mantle heterogeneities, geoid, and plate motion: A Monte Carlo inversion, Journal of Geophysical Research: Solid Earth, 94, 13 739–13 754, 1989.

Richter, F. M.: Convection and the large-scale circulation of the mantle, Journal of Geophysical Research, 78, 8735–8745, 1973.

Ruh, J. B., Le Pourhiet, L., Agard, P., Burov, E., and Gerya, T.: Tectonic slicing of subducting oceanic crust along plate interfaces: Numerical modeling, Geochemistry, Geophysics, Geosystems, 16, 3505–3531, 2015.

Schmalholz, S., Podladchikov, Y., and Schmid, D.: A spectral/finite difference method for simulating large deformations of heterogeneous, viscoelastic materials, Geophysical Journal International, 145, 199–208, 2001.

Schmalholz, S. M. and Fletcher, R. C.: The exponential flow law applied to necking and folding of a ductile layer, Geophysical Journal International, 184, 83–89, 2011.

Schmalholz, S. M. and Mancktelow, N. S.: Folding and necking across the scales: a review of theoretical and experimental results and their applications., Solid Earth, 7, 2016.

Schmalholz, S. M., Podladchikov, Y. Y., and Jamtveit, B.: Structural softening of the lithosphere, Terra Nova, 17, 66–72, 2005.

Schmalholz, S. M., Duretz, T., Hetényi, G., and Medvedev, S.: Distribution and magnitude of stress due to lateral variation of gravitational potential energy between Indian lowland and Tibetan plateau, Geophysical Journal International, 216, 1313–1333, 2019.

Schmid, S., Boland, J., and Paterson, M.: Superplastic flow in finegrained limestone, Tectonophysics, 43, 257–291, 1977.

Schubert, G., Turcotte, D. L., and Olson, P.: Mantle convection in the Earth and planets, Cambridge University Press, 2001.

Stern, R. J.: Subduction initiation: spontaneous and induced, Earth and Planetary Science Letters, 226, 275–292, 2004.

Stern, R. J. and Gerya, T.: Subduction initiation in nature and models: A review, Tectonophysics, 746, 173–198, 2018.

Tackley, P. J., Schubert, G., Glatzmaier, G. A., Schenk, P., Ratcliff, J. T., and Matas, J.-P.: Three-dimensional simulations of mantle convection in Io, Icarus, 149, 79–93, 2001.

Thielmann, M. and Kaus, B. J.: Shear heating induced lithospheric-scale localization: Does it result in subduction?, Earth and Planetary Science Letters, 359, 1–13, 2012.

Torrance, K. and Turcotte, D.: Structure of convection cells in the mantle, Journal of Geophysical Research, 76, 1154–1161, 1971.

Tosi, N., Stein, C., Noack, L., Hüttig, C., Maierova, P., Samuel, H., Davies, D. R., Wilson, C. R., Kramer, S. C., Thieulot, C., et al.: A
community benchmark for viscoplastic thermal convection in a 2-D square box, Geochemistry, Geophysics, Geosystems, 16, 2175–2196,
2015.

Trubitsyn, V. and Trubitsyna, A.: Effects of compressibility in the mantle convection equations, Izvestiya, Physics of the Solid Earth, 51,
801–813, 2015.

Turcotte, D. and Schubert, G.: Geodynamics, Cambridge University Press, 2014.

White, S. t. and Knipe, R.: Transformation-and reaction-enhanced ductility in rocks, Journal of the Geological Society, 135, 513–516, 1978.

Wilson, J. T.: Did the Atlantic close and then re-open?, Nature, 211, 676–681, 1966.

Wilson, R., Houseman, G., Buiter, S., McCaffrey, K., and Doré, A.: Fifty years of the Wilson Cycle concept in plate tectonics: an overview,
2019.

Workman, R. K. and Hart, S. R.: Major and trace element composition of the depleted MORB mantle (DMM), Earth and Planetary Science
Letters, 231, 53–72, 2005.

Yamato, P., Duretz, T., May, D. A., and Tartese, R.: Quantifying magma segregation in dykes, Tectonophysics, 660, 132–147, 2015.

Yamato, P., Duretz, T., and Angiboust, S.: Brittle/ductile deformation of eclogites: insights from numerical models, Geochemistry, Geo-
physics, Geosystems, 2019.

Yang, F., Santosh, M., Tsunogae, T., Tang, L., and Teng, X.: Multiple magmatism in an evolving suprasubduction zone mantle wedge: the
case of the composite mafic–ultramafic complex of Gaositai, North China Craton, Lithos, 284, 525–544, 2017.

Zahnle, K. J., Kasting, J. F., and Pollack, J. B.: Evolution of a steam atmosphere during Earth's accretion, Icarus, 74, 62–97, 1988.

Zhao, Z., Bons, P., Wang, G., Soesoo, A., and Liu, Y.: Tectonic evolution and high-pressure rock exhumation in the Qiangtang terrane, central
Tibet, Solid Earth, 6, 457, 2015.

Zhou, X., Li, Z.-H., Gerya, T. V., and Stern, R. J.: Lateral propagation–induced subduction initiation at passive continental margins controlled
by preexisting lithospheric weakness, Science Advances, 6, eaaz1048, 2020.
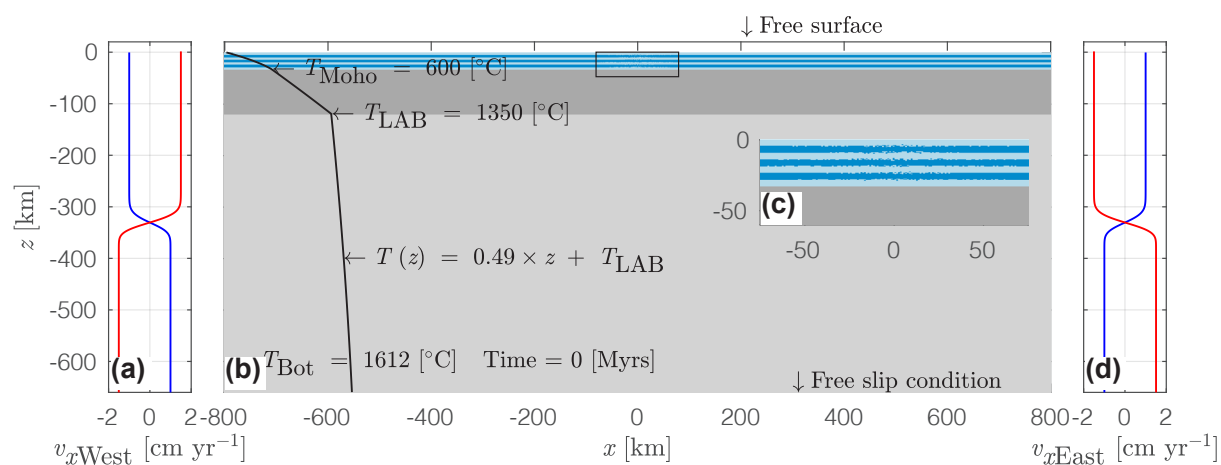
Figure 1. Model configuration and boundary conditions. Dark blue colours represent strong and light blue colours represent weak crustal units, dark grey colours represent the mantle lithosphere and light grey colours the upper mantle. (a) Profile of horizontal velocity for material inflow and outflow along the left vertical boundary. Blue colour indicates the profile for the extension and red colour the profile for the convergence, respectively, (b) entire model domain including the material phases (colour-code as explained above) and initial vertical temperature profile (black line), (c) enlargement of the centre of the model domain showing the initial random perturbation on the horizontal mechanical layer interfaces used to localise deformation in the centre of the domain and (d) is the same profile as shown in (a), but along the right vertical boundary.
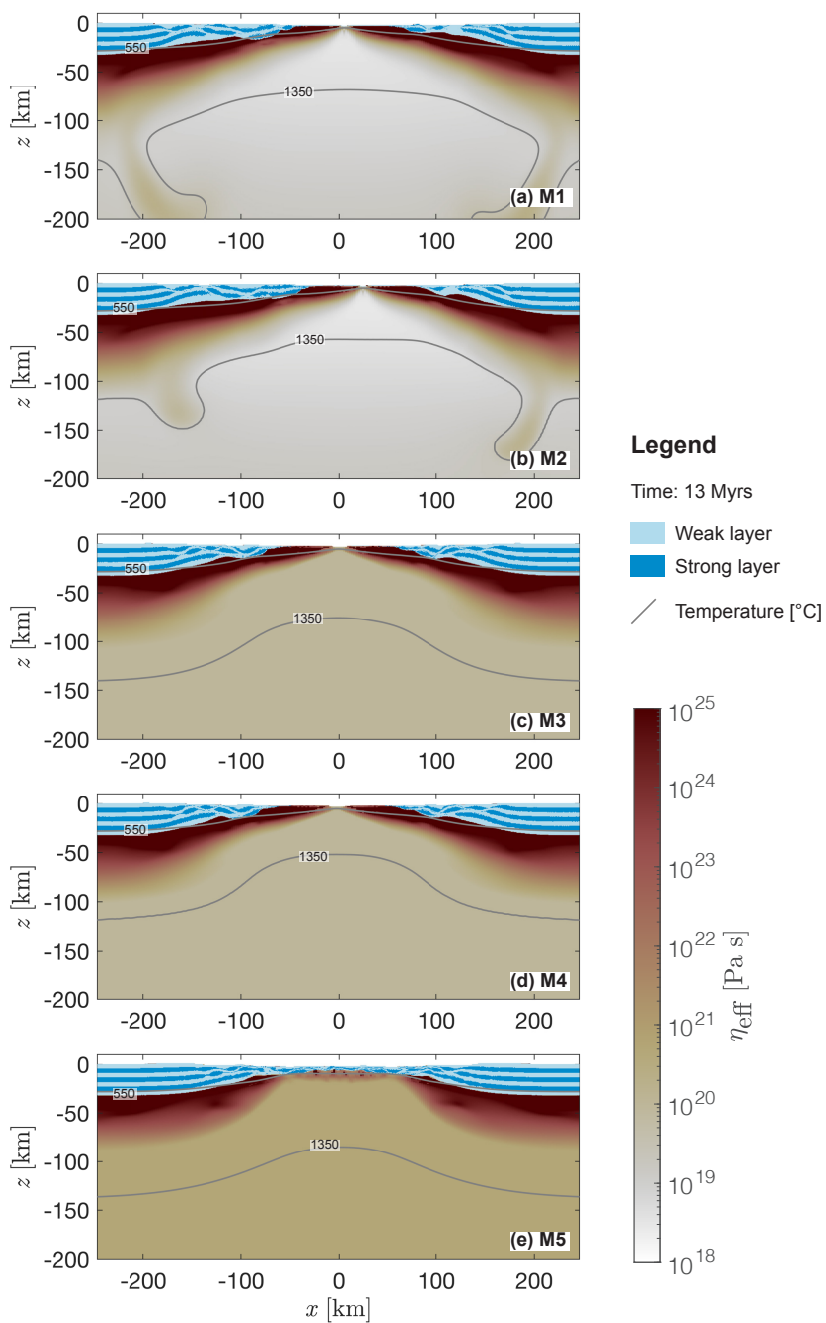
Figure 2. (a)-(e) Enlargements of results of models M1-5 at 13 Myrs of modelled time. Blue colours indicate mechanically weak (light) and strong (dark) crustal units. White to red colours show the effective viscosity field calculated by the numerical algorithm on a logarithmic scale for the lithospheric mantle and the upper mantle. Grey lines show the level of 550 and 1350 °C isotherm.
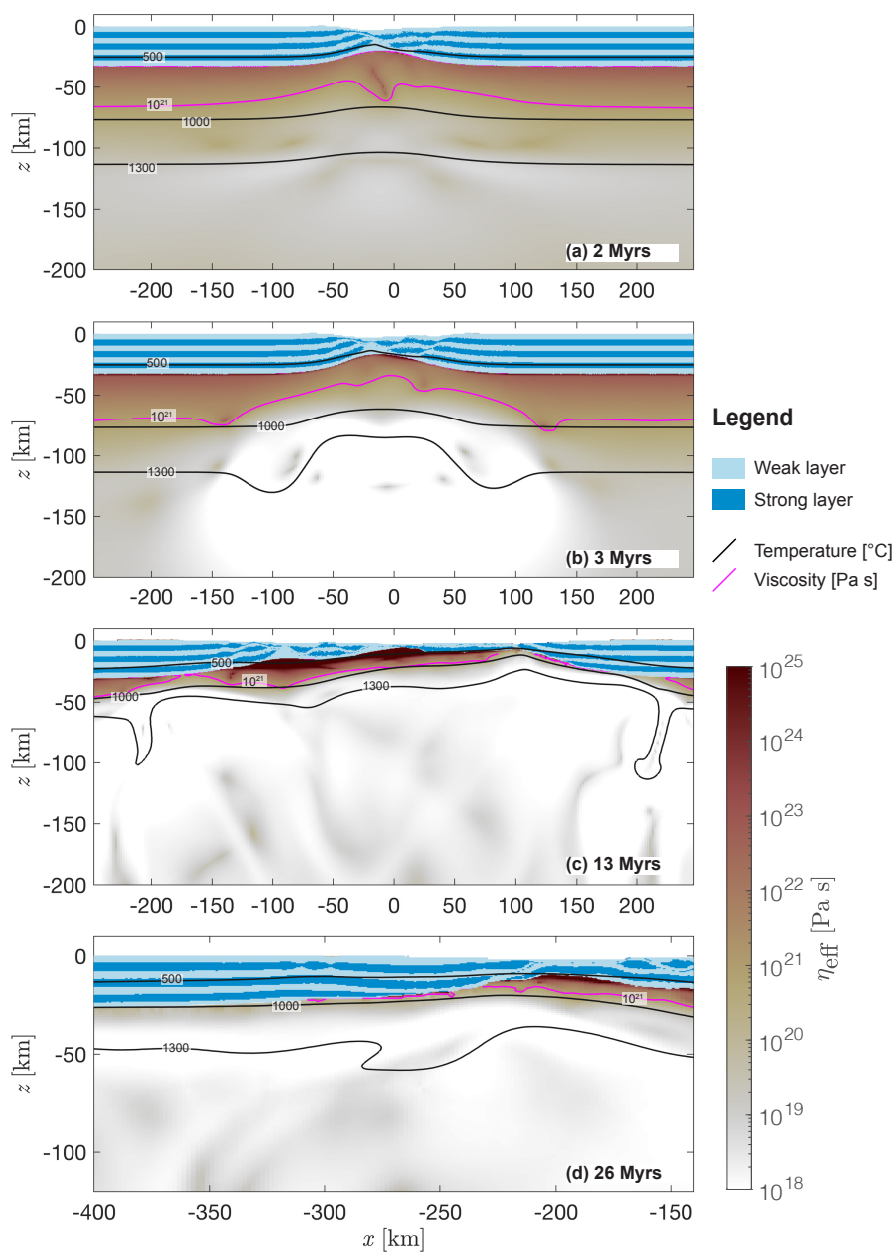
Figure 3. Evolution of model M6 with wet olivine flow law at (a) 2 Myrs, (b) 3 Myrs, (c) 13 Myrs and (d) 26 Myrs. Blue colours indicate mechanically weak (light) and strong (dark) crustal units. White to red colours show the effective viscosity field calculated by the numerical algorithm on a logarithmic scale for the lithospheric mantle and the upper mantle. Grey lines show the level of 500, 1000 and 1350 °C isotherm and the magenta coloured line shows the level of the 10^{21} Pa s viscosity isopleth. This contour line represents the mechanical boundary between the mantle lithosphere and the convecting upper mantle.
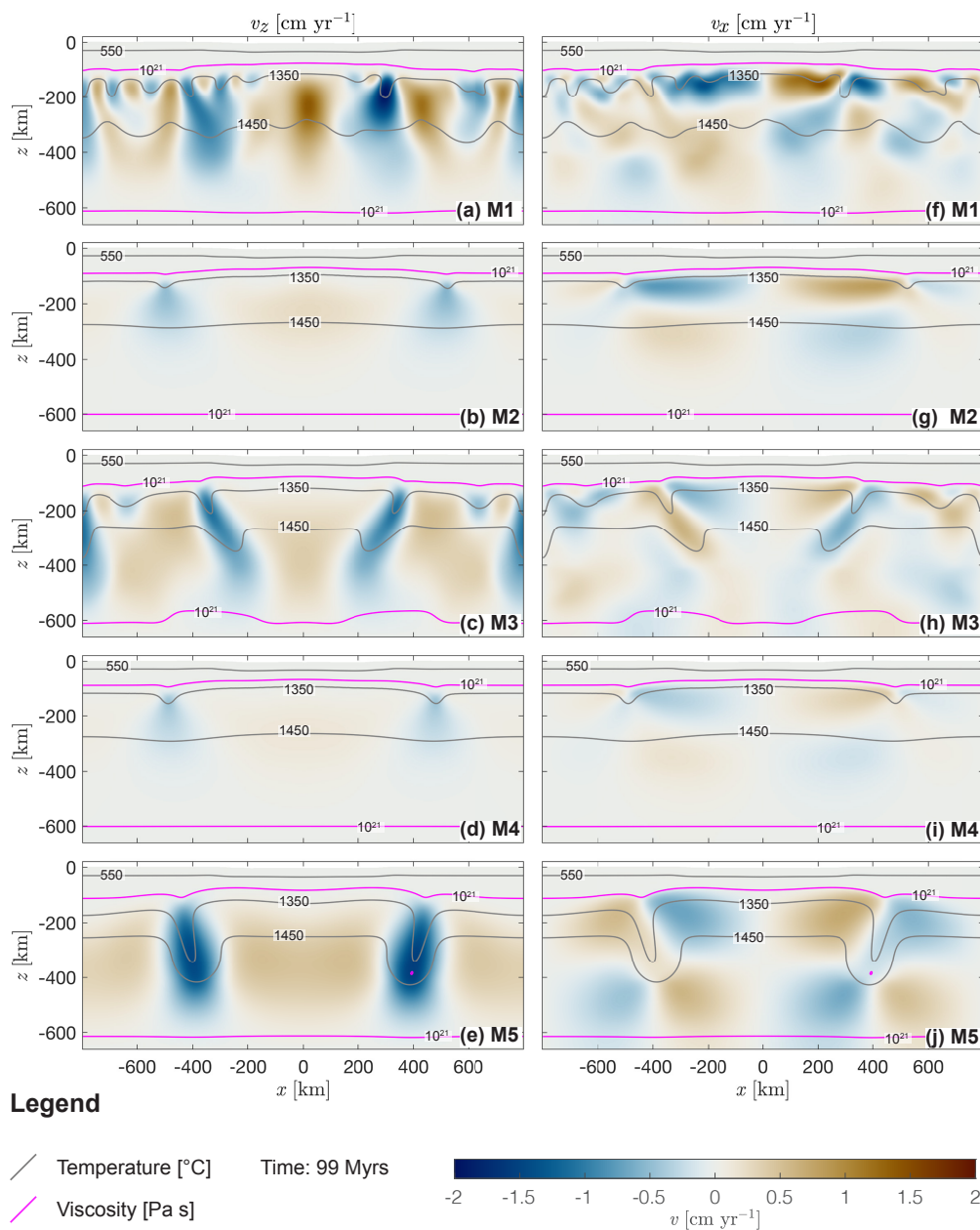
Figure 4. Results of models M1-5 at 99 Myrs (end of thermal relaxation period). (a)-(e) Vertical velocity field, (f)-(j) horizontal velocity field. Blue to red colour indicate the velocity magnitudes calculated by the numerical algorithm. Grey lines show the level of the 550, 1350 and 1450 °C isotherms and the magenta coloured line shows the level of the 10^{21} Pa s viscosity isopleth. This contour line represents the mechanical boundary between the mantle lithosphere and the convecting upper mantle.
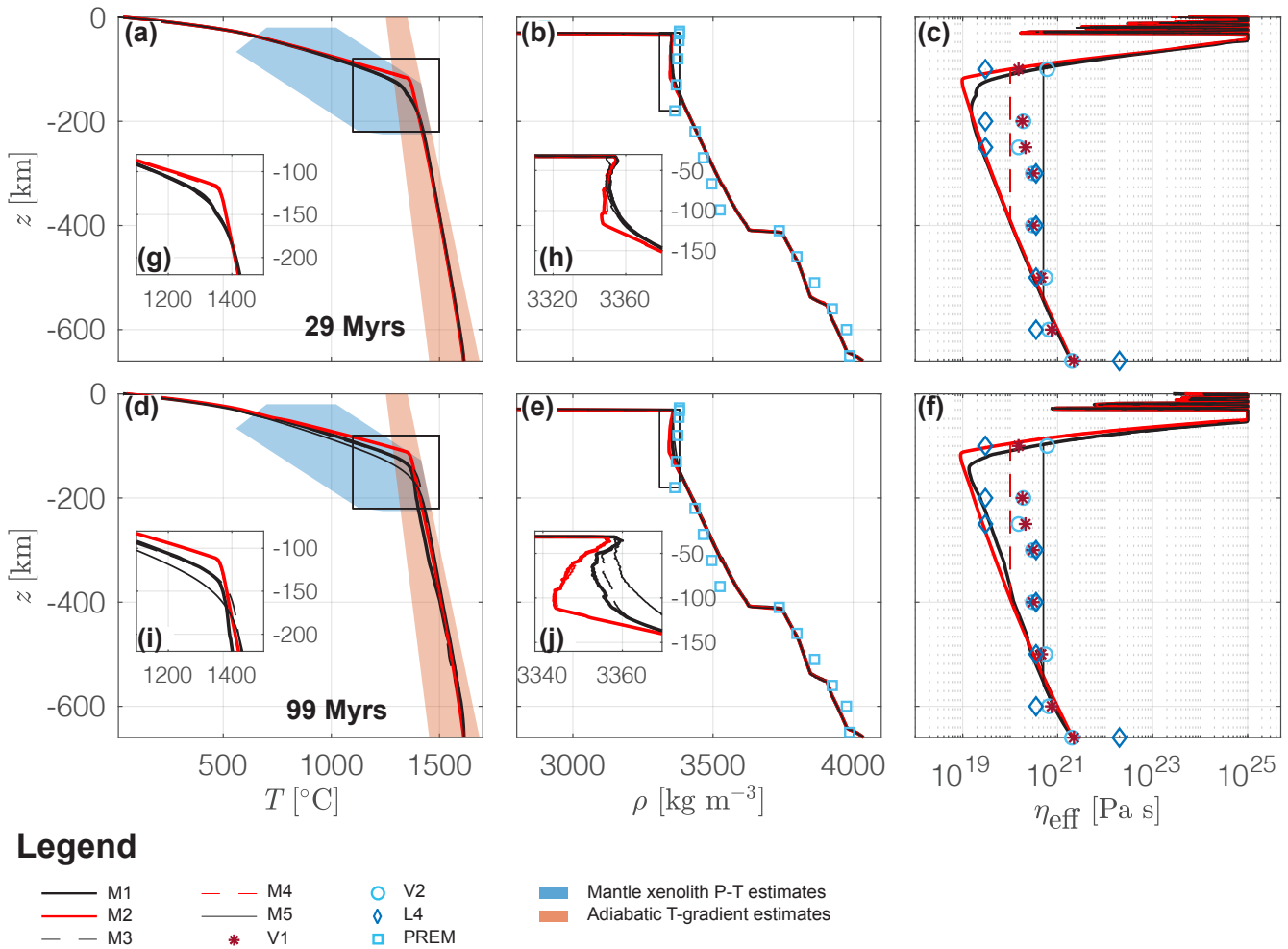
Figure 5. Horizontally averaged vertical profiles of temperature, T, density, ρ, and effective viscosity, η_{eff}. Top row: after 29 Myrs, bottom row: after 99 Myrs in model history. (a) and (d) show horizontally averaged temperature, (b) and (e) show horizontally averaged density and (c) and (f) show horizontally averaged viscosity. (g)-(h) show an enlarged region of the parental subfigure. Black and red, solid and dashed lines show the results of models M1-5. In (a) and (d): blue area indicates P-T condition estimates from mantle xenolith data and orange area indicates estimates for a range of adiabatic gradients both taken from Hasterok and Chapman (2011) (fig. 5). Estimates for adiabatic temperature gradients are extrapolated to 660 km depth. In (b) and (e): squares indicate density estimates from the preliminary reference Earth model (PREM) (Dziewonski and Anderson, 1981). In (c) and (f): circles and stars indicate viscosity profiles inferred from Occam-style inversion of glacial isostatic adjustment and convection related data originally by Mitrovica and Forte (2004), diamonds show a four-layer model fit of mantle flow to seismic anisotropy originally by Behn et al. (2004). All profiles taken from Forte et al. (2010) (fig. 2). The median is used as statistical quantity for averaging, because it is less sensitive to extreme values compared to the arithmetic mean.
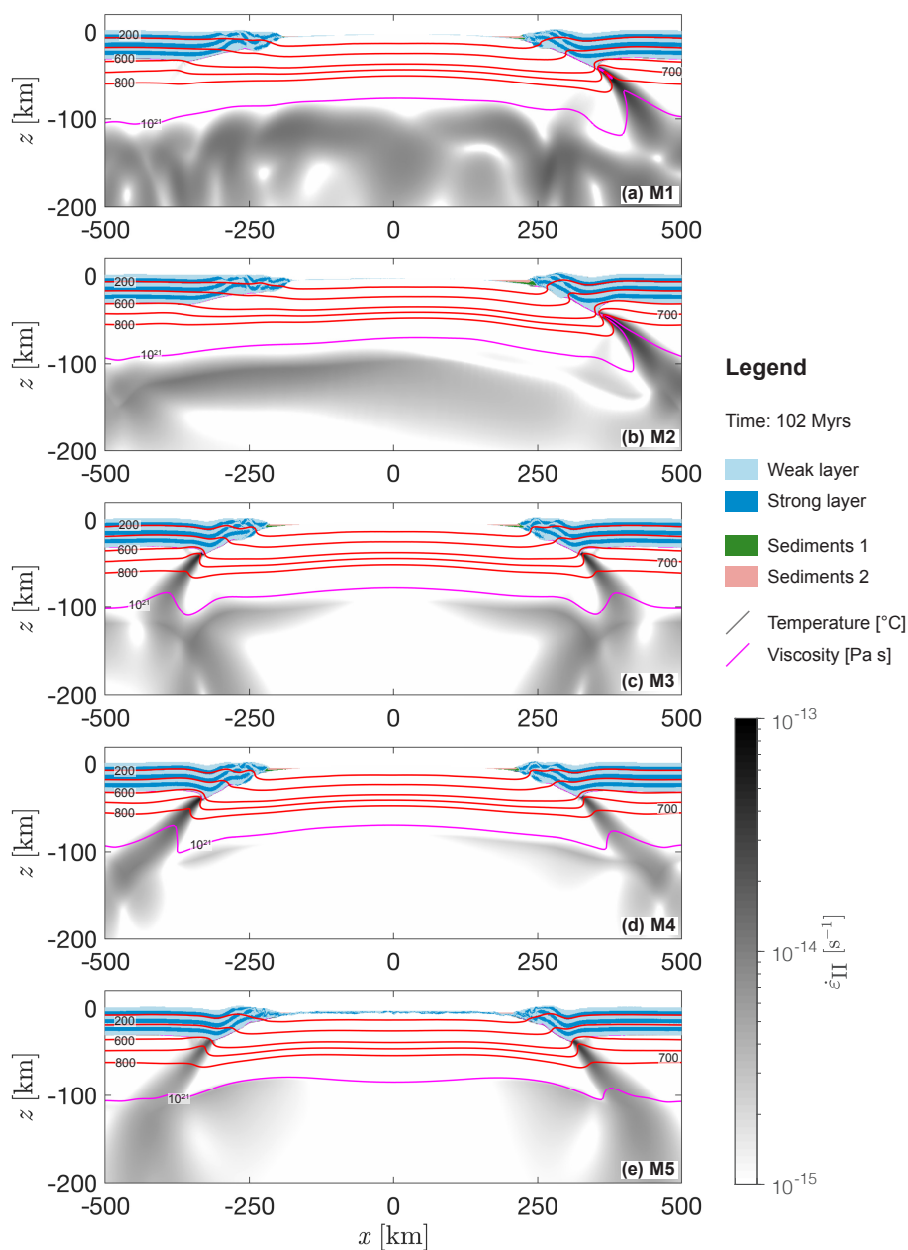
Figure 6. (a)-(e) Results of models M1-5 after 102 Myrs of simulated deformation. Blue colours indicate mechanically weak (light) and strong (dark) crustal units, red and salmon colours indicate the sedimentary units (only minor volumes in trench regions). White to black colours indicate the second invariant of the strain rate tensor field calculated by the numerical algorithm on a logarithmic scale. Red lines show levels of several isotherms and the magenta coloured line shows the level of the 10^{21} Pa s viscosity isopleth. This contour line represents approximately the mechanical transition between the mantle lithosphere and the convecting upper mantle.
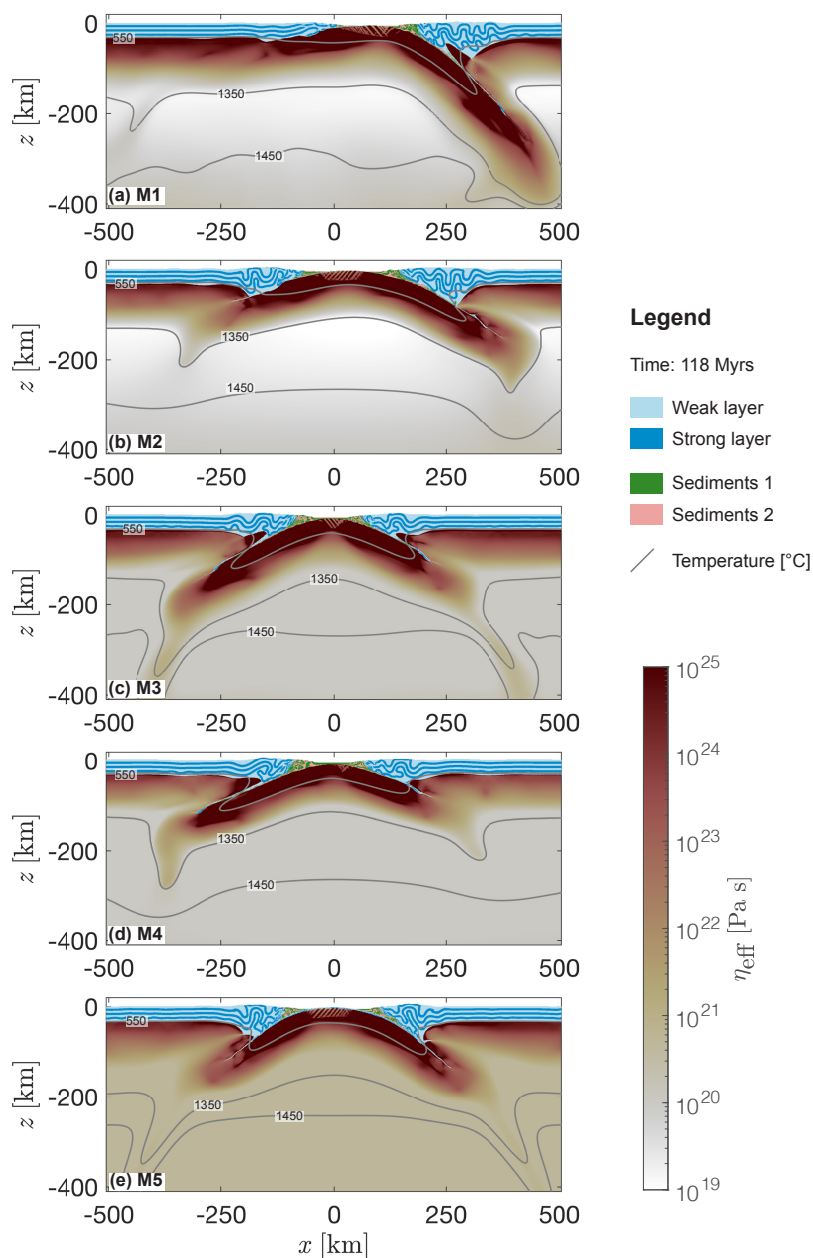
Figure 7. (a)-(e) Results of models M1-5 after 118 Myrs of simulated deformation. Blue colours indicate mechanically weak (light) and strong (dark) crustal units, red and salmon colours indicate the sedimentary units. White to red colours show the effective viscosity field calculated by the numerical algorithm on a logarithmic scale for the mantle lithosphere and the upper mantle. Grey lines show the level of the 550, 1350 and 1450 °C isotherm.
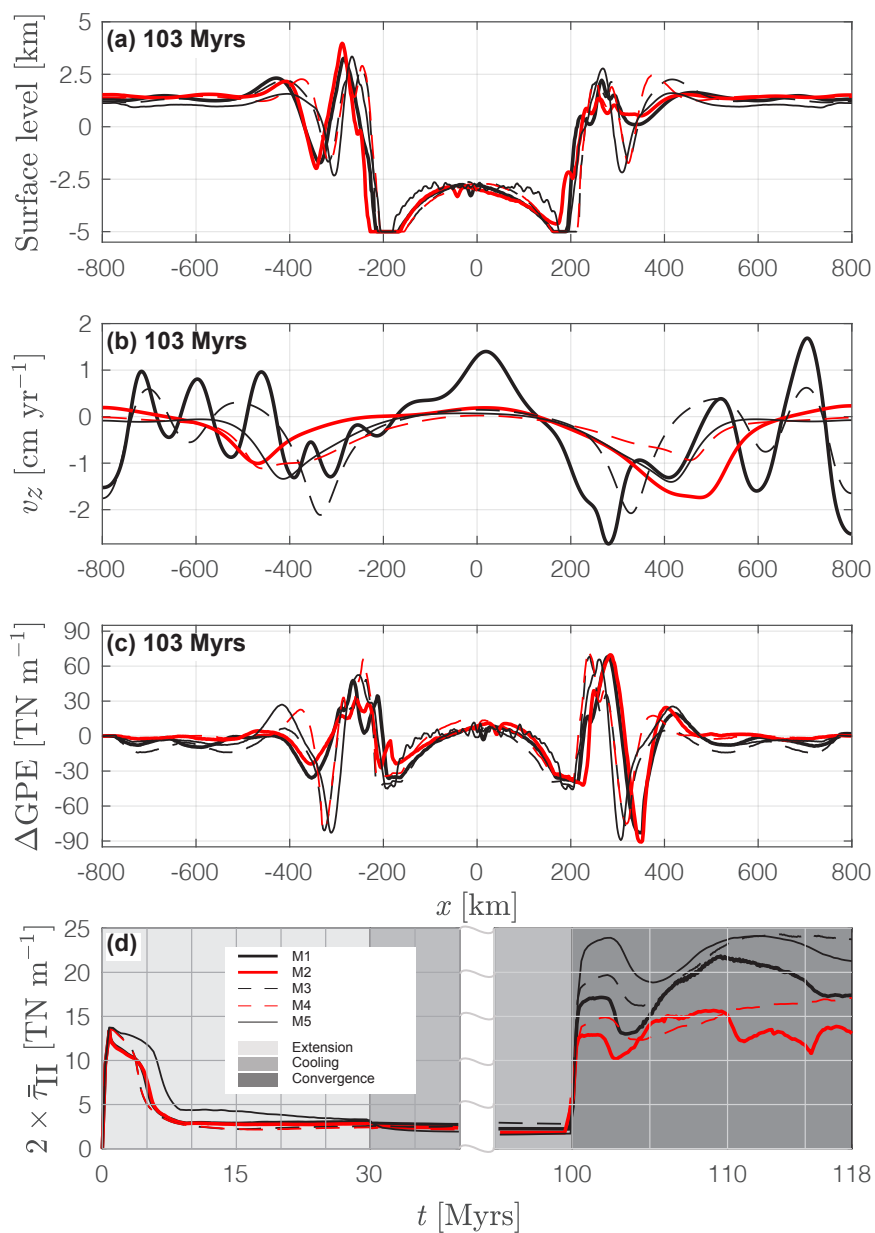
Figure 8. (a) Model topography, (b) horizontal profile of vertical velocity at a depth of 175 km and (c) difference in gravitational potential energy of models M1-5 after 103 Myrs. (d) Vertical integral of two times the second invariant of the deviatoric stress tensor ($\bar{\tau}_{II}$, see appendix D) through the entire model time. Grey regions indicate stage of extension (light grey), thermal relaxation (grey) and convergence (dark grey). The thermal relaxation period is not entirely displayed, because values for $\bar{\tau}_{II}$ remain constant when no deformation is applied to the system. The legend shown in (d) is valid for all panels above as well.
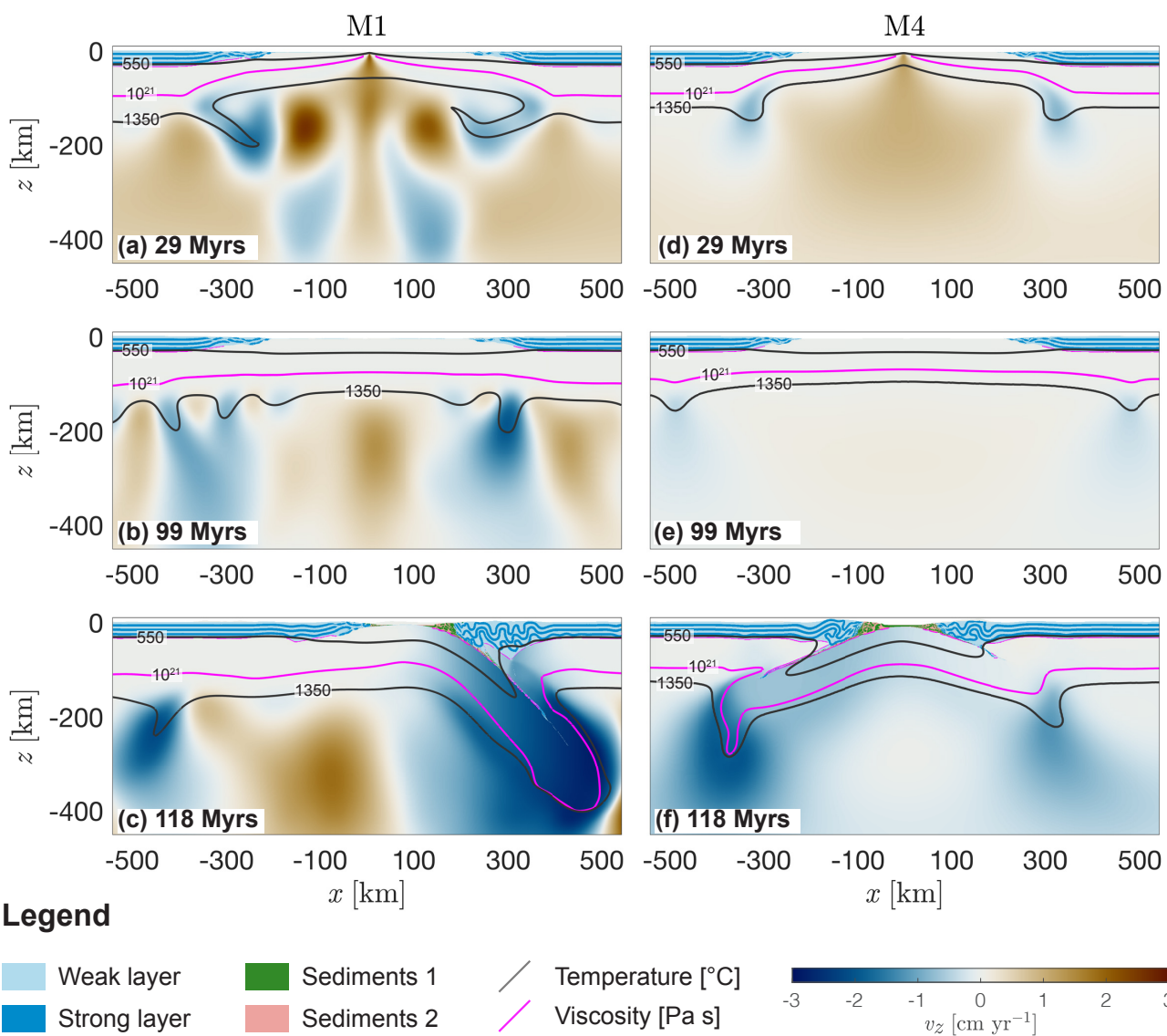
Figure 9. Comparison of vertical velocity fields of models M1 (left column) and M4 (right column) at: (a) and (d) the end of rifting, (b) and (e) end of thermal relaxation period and (c) and (d) during subduction. Blue to red colours indicate velocity values and black lines indicate the level of the 550 and 1350 °C isotherm. The magenta contour indicates the level of the 10^{21} Pa s isopleth which represents approximately the mechanical transition between the mantle lithosphere and the convecting upper mantle.
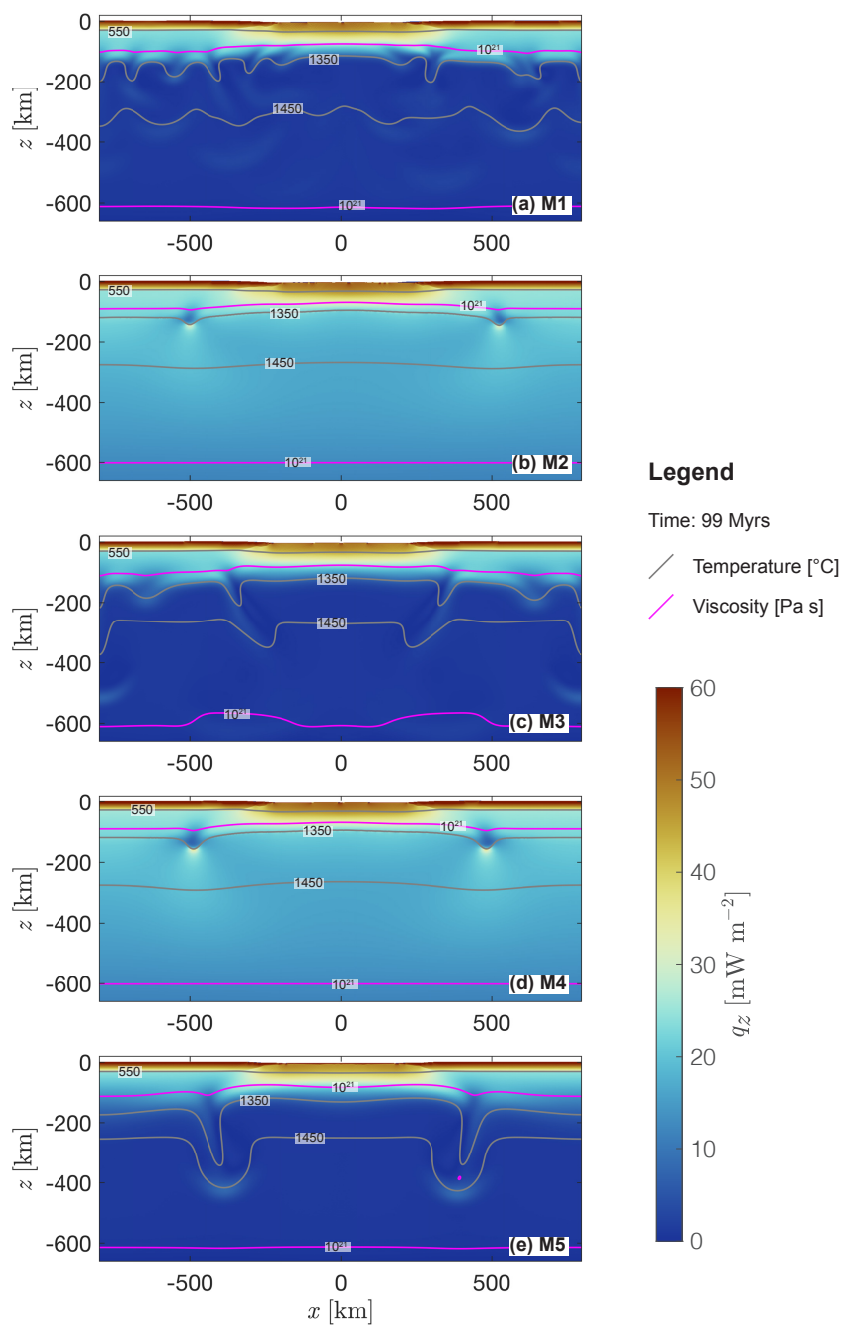
Figure 10. Vertical conductive heat flow represented by blue to red colours for models M1-5 ((a)-(e)) after 99 Myrs. The grey lines indicate the depth of the 550, 1350 and 1450 °C isotherm. The magenta line indicates the depth of the 10^{21} Pa s isopleth which represents approximately the mechanical transition between the mantle lithosphere and the convecting upper mantle.
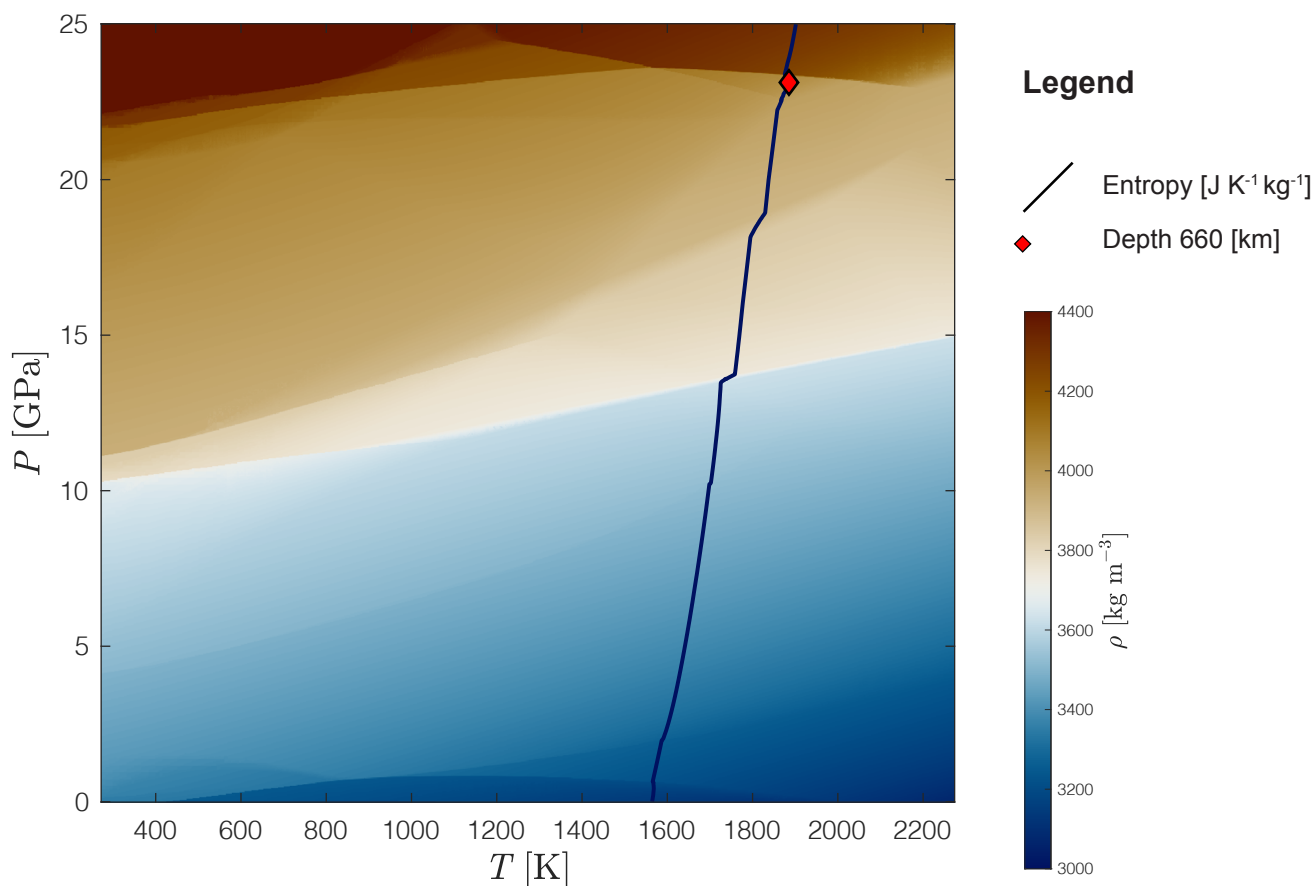
Figure A1. Hawaiian pyrolite phase diagram calculated with Perple_X (Connolly, 2005). Bulk rock composition in weight amount: 44.71 (SiO_2), 3.98 (Al_2O_3), 8.18 (FeO), 38.73 (MgO), 3.17 (CaO) and 0.13 (Na_2O). Bulk rock composition taken from Workman and Hart (2005). Blue to red colours indicate density calculated for the given pressure and temperature range, black line indicates the isentrop for a temperature of 1350 °C at the base of a 120 km thick lithosphere and the red diamond shows the pressure and temperature conditions at 660 km depth following this isentrop.
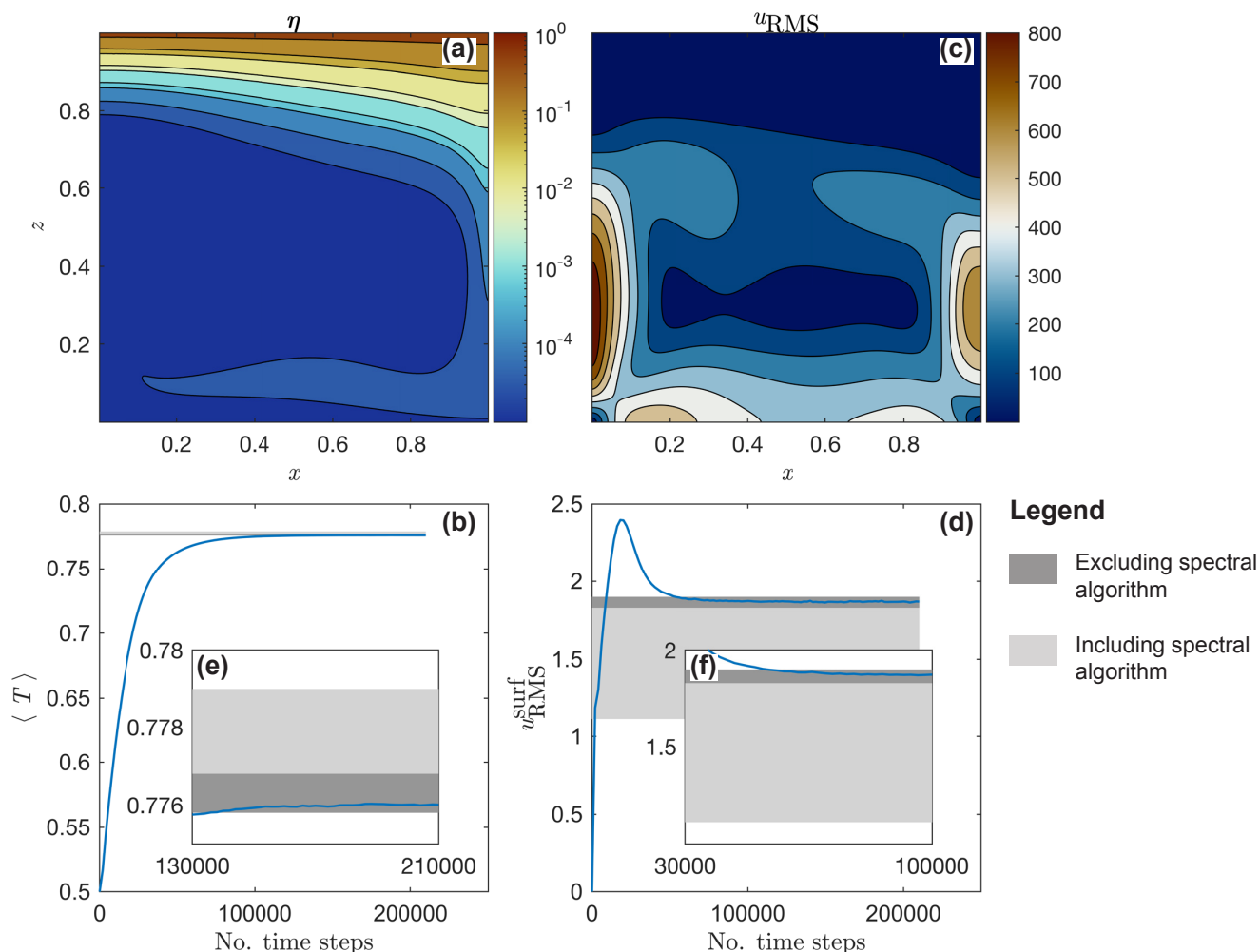
Figure A2. Results of 2D convection benchmark. (a) effective viscosity on logarithmic scale after convection reached a steady state, (b) normal average temperature calculated as in eq. C6 for the entire model history, (c) root mean square velocity field for the entire domain after convection reached a steady state, (d) root mean square velocity at the surface of the modelled domain of the entire model history calculated as in eq. C7, (e) normal average temperature calculated as in eq. C6 for the time period at which the convection reaches a steady state and (f) root mean square velocity at the surface of the modelled domain calculated as in eq. C7 for the time period at which the convection reaches a steady state. In fig. A2(b) and fig. A2(d)-(f), the dark grey area only shows the range of minimum maximum values for the given diagnostic quantity obtained by the algorithms tested by Tosi et al. (2015) excluding the spectral algorithm. Dark combined with light grey areas indicate the range obtained by all algorithms tested by Tosi et al. (2015) including the spectral algorithm.